Dartmouth College
Dartmouth Digital Commons

Open Dartmouth: Faculty Open Access Articles

9-17-2012

Contribution of the Accretion Disk, Hot Corona, and Obscuring Torus to the Luminosity of Seyfert Galaxies: Integral and Spitzer Observations

S. Sazonov
Russian Academy of Sciences

S. P. Willner
Harvard-Smithsonian Center for Astrophysics

A. D. Goulding
Harvard-Smithsonian Center for Astrophysics

R. C. Hickox
Dartmouth College

Follow this and additional works at: https://digitalcommons.dartmouth.edu/facoa

Part of the External Galaxies Commons

CONTRIBUTION OF THE ACCRETION DISK, HOT CORONA, AND OBSCURING TORUS TO THE LUMINOSITY OF SEYFERT GALAXIES: *INTEGRAL* AND *SPITZER* OBSERVATIONS

S. Sazonov[1,2], S. P. Willner[3], A. D. Goulding[3], R. C. Hickox[4], V. Gorjian[5], M. W. Werner[5], E. Churazov[1,2], R. Krivonos[1,2], M. Revnivtsev[1], R. Sunyaev[1,2], C. Jones[3], S. S. Murray[3,6], A. Vikhlinin[1,3], A. C. Fabian[7], AND W. R. Forman[2]

[1] Space Research Institute, Russian Academy of Sciences, Profsoyuznaya 84/32, Moscow 117997, Russia
[2] Max-Planck-Institut für Astrophysik, Karl-Schwarzschild-Str. 1, D-85741 Garching, Germany
[3] Harvard-Smithsonian Center for Astrophysics, 60 Garden Street, Cambridge, MA 02138, USA
[4] Department of Physics and Astronomy, Dartmouth College, 6127 Wilder Laboratory, Hanover, NH 03755, USA
[5] Jet Propulsion Laboratory, California Institute of Technology, MS 169-327, 4800 Oak Grove Drive, Pasadena, CA 91109, USA
[6] Department of Physics and Astronomy, Johns Hopkins University, Baltimore, MD 21218, USA
[7] Institute of Astronomy, Madingley Road, Cambridge CB3 0HA, UK
Received 2012 May 11; accepted 2012 August 20; published 2012 September 17

ABSTRACT

We estimate the relative contributions of the supermassive black hole (SMBH) accretion disk, corona, and obscuring torus to the bolometric luminosity of Seyfert galaxies, using *Spitzer* mid-infrared (MIR) observations of a complete sample of 68 nearby active galactic nuclei (AGNs) from the *INTEGRAL* all-sky hard X-ray (HX) survey. This is the first HX-selected (above 15 keV) sample of AGNs with complementary high angular resolution, high signal-to-noise, MIR data. Correcting for the host galaxy contribution, we find a correlation between HX and MIR luminosities: $L_{15\,\mu m} \propto L_{HX}^{0.74\pm0.06}$. Assuming that the observed MIR emission is radiation from an accretion disk reprocessed in a surrounding dusty torus that subtends a solid angle decreasing with increasing luminosity (as inferred from the declining fraction of obscured AGNs), the intrinsic disk luminosity, L_{Disk}, is approximately proportional to the luminosity of the corona in the 2–300 keV energy band, L_{Corona}, with the L_{Disk}/L_{Corona} ratio varying by a factor of 2.1 around a mean value of 1.6. This ratio is a factor of ~2 smaller than for typical quasars producing the cosmic X-ray background. Therefore, over three orders of magnitude in luminosity, HX radiation carries a large, and roughly comparable, fraction of the bolometric output of AGNs. We estimate the cumulative bolometric luminosity density of local AGNs at ~$(1–3) \times 10^{40}$ erg s^{-1} Mpc^{-3}. Finally, the Compton temperature ranges between $kT_c \approx 2$ and ≈ 6 keV for nearby AGNs, compared to $kT_c \approx 2$ keV for typical quasars, confirming that radiative heating of interstellar gas can play an important role in regulating SMBH growth.

Key words: accretion, accretion disks – black hole physics – galaxies: active – galaxies: Seyfert – infrared: galaxies – X-rays: galaxies

Online-only material: color figures

1. INTRODUCTION

Active galactic nuclei (AGNs) are extremely powerful sources of electromagnetic radiation over many decades in frequency from radio waves to gamma rays. According to the commonly accepted scenario, an AGN shines due to accretion of gas onto a supermassive black hole (SMBH) residing in a galactic nucleus.

In Seyfert galaxies and quasars, most of the luminosity is emitted in the form of ultraviolet (UV) radiation generated in a geometrically thin, optically thick accretion disk (Shakura & Sunyaev 1973), giving rise to a "big blue bump" (BBB) in the spectral energy distribution (SED; e.g., Malkan & Sargent 1982). Additional, higher energy radiation is generated in a hot corona of the accretion disk (e.g., Haardt & Maraschi 1993) and possibly also in collimated outflows (jets) of relativistic plasma, producing a hard X-ray (HX) peak in the SED. The integrated (and redshifted) HX emission of all AGNs in the observable universe makes up the bulk of the cosmic X-ray background (CXB). There is also a third, mid-infrared (MIR) peak in AGN SEDs (e.g., Barvainis 1987), which arises from reprocessing of a significant fraction of the disk's and some of the coronal radiation in a torus of molecular gas and dust surrounding the inner accretion flow. In fact, only in unobscured or "type 1" AGNs can all three spectral components, the HX bump, the BBB, and the MIR bump, be observed. According to

the unified model (Antonucci 1993), these are objects viewed through the funnel of the dusty torus. In contrast, only the HX and MIR components are visible in the SEDs of obscured or "type 2" AGNs because the torus is opaque to UV emission from the accretion disk but transparent to coronal radiation at energies above ~15 keV (except in Compton-thick sources) and to its own infrared emission (at least at wavelengths $\gtrsim 20\,\mu m$). All other emission components, including broad- and narrow-line emission and non-thermal radio and gamma-ray radiation, are usually not significant as regards their contribution to the angular-integrated bolometric luminosity of AGNs; these components will therefore not be discussed below.

To understand how electromagnetic radiation is emitted and reprocessed during accretion of matter onto SMBHs, it is crucial to explore (1) in what proportion the AGN luminosity is shared between the accretion disk and its corona, (2) what fraction of the bolometric luminosity is reprocessed in the torus, and (3) how these properties depend on black hole mass and accretion rate. One also needs such information to study the role of AGN feedback in regulating SMBH growth and galactic evolution. One of the proposed feedback mechanisms is photoionization and Compton heating of interstellar gas by AGN radiation (e.g., Ciotti & Ostriker 2001; Proga et al. 2008), whose efficiency critically depends on the AGN SED (Sazonov et al. 2004, 2005). Finally, information on AGN SEDs can be used to

derive bolometric corrections required to reconstruct the cosmic history of SMBH accretion growth based on AGN statistics provided by extragalactic surveys (e.g., Marconi et al. 2004; Merloni & Heinz 2008).

Among all types of AGNs, the SEDs of unobscured high-luminosity quasars have been studied most extensively (see, e.g., Elvis et al. 1994; Richards et al. 2006; Shang et al. 2011). Their obscured counterparts—type 2 quasars—have been explored to a much lesser degree, although recent surveys have begun to find such objects in significant numbers (e.g., Polletta et al. 2006; Hickox et al. 2007; Lanzuisi et al. 2009). There is also much uncertainty with respect to the SEDs of Seyfert galaxies, which are typically less luminous than more distant quasars. The difficulty is that even in Seyfert 1s, the accretion disk emission is usually contaminated by host galaxy stellar emission in visible bands and the BBB peaks in the observationally difficult far-UV band (see, however, Scott et al. 2004; Vasudevan & Fabian 2007, 2009).

The goal of the present study is to systematically assess the relative contributions of the accretion disk, hot corona, and obscuring torus to the bolometric luminosity of local Seyfert galaxies. To this end, we (1) cross-correlate the HX luminosities of nearby AGNs detected during the all-sky survey of the *International Gamma-Ray Astrophysics Laboratory* (*INTEGRAL*; Winkler et al. 2003) with the MIR luminosities of these objects measured by the *Spitzer Space Telescope* (Werner et al. 2004) and (2) use the proportion of obscured to unobscured AGNs to estimate the opening angle of dusty tori as a function of luminosity. We then put our findings for nearby AGNs into the broader context of cosmic SMBH growth by making a comparison with distant quasars.

Most previous relevant studies were based on AGN samples compiled in a fairly arbitrary manner from optical and/or soft X-ray (below 10 keV) catalogs (e.g., Lutz et al. 2004; Horst et al. 2006; Hönig et al. 2010). In these energy bands, AGNs can easily be missed due to absorption, as powerful sources can become invisible when obscured by large amounts of dust and cold gas in the torus and/or host galaxy. Furthermore, as already noted above, optical emission from relatively low luminosity AGNs (LLAGNs) can be diluted against the background of a luminous galaxy (see Mushotzky 2004 for a detailed discussion of AGN selection at different wavelengths).

The HX band, above $\sim$15 keV, provides a census of AGNs that is far less biased with respect to the viewing orientation of the torus and is unbiased with respect to host galaxy properties. There have been a few previous attempts (Vasudevan et al. 2010; Mullaney et al. 2011) of systematically studying the MIR properties of HX-selected AGNs using the *Swift* all-sky HX survey (Tueller et al. 2010). However, these studies either used data from the *IRAS* all-sky photometric infrared survey, so that it was impossible to reliably subtract the host galaxy contribution from the AGN emission, or used high angular resolution *Spitzer* data but only for statistically incomplete subsamples of *Swift* AGNs. Our *INTEGRAL* sample is the first statistically complete, HX-selected sample of AGNs with complementary high angular resolution, high signal-to-noise, MIR data. The extensive *Spitzer* coverage (3.6–38 μm) available for the entire *INTEGRAL* sample makes this a unique data set for studying SEDs of AGNs in the local universe.

2. *INTEGRAL* AGN SAMPLE

Our study is based on the complete sample of AGNs (Krivonos et al. 2007; Sazonov et al. 2007) detected in the 17–60 keV energy band by the IBIS/ISGRI detector (Ubertini et al. 2003) aboard *INTEGRAL* during the first three and a half years of the mission, from 2002 October until 2006 June. These observations compose a serendipitous all-sky HX survey with the flux limit varying by a factor of a few over the sky. We have excluded from the present analysis blazars (flat-spectrum radio quasars and BL Lac objects), a relatively rare subclass of AGNs whose observed emission is believed to be dominated by a narrow, strongly collimated component. We have also excluded AGNs located in the "zone of avoidance" near the Galactic plane ($|b| < 5°$) because there remain unidentified *INTEGRAL* sources in this region of the sky, while we wish our sample to be nearly 100% complete to minimize selection effects.

The resulting set comprises 68 AGNs (Table 1). In the first seven columns of Table 1 we have collected information on optical/radio AGN types, distances, HX fluxes and luminosities, and X-ray absorption column densities (N_H). These data are mostly adopted from the original *INTEGRAL* catalog (Krivonos et al. 2007; Sazonov et al. 2007) although some updates take into account follow-up observations carried out since publication of the catalog. In particular, thanks to recent X-ray observations by *Chandra*, *Swift*, and *XMM-Newton*, all of the previously missing N_H values have now been estimated. All the reported absorption columns may be considered reliable because they are based on high signal-to-noise X-ray spectroscopic data. We do not quote the uncertainties associated with the N_H values because the information on absorption columns has been compiled from various sources and in most cases the actual uncertainty is likely dominated by systematic effects associated with the particular spectral modeling procedure used. In fact, multiple measurements taken for some AGNs at different times and/or by different instruments sometimes yield N_H values that differ from each other by more than their reported uncertainties. We estimate that the total uncertainties associated with N_H columns for our sources are typically smaller than 30% and do not affect the present study in any significant way.

All but one of our AGNs are located at low redshift ($z < 0.1$, the most distant one, IGR J09446$-$2636, being at $z = 0.14$). For 18 nearby (closer than $\sim$40 Mpc) Seyfert galaxies we have adopted distance estimates from either Tully et al. (2009) or Tully (1988); otherwise, luminosity distances have been calculated from the spectroscopic redshifts assuming a cosmology with $\Omega_m = 0.3$, $\Omega_\Lambda = 0.7$, and $H_0 = 72$ km s^{-1} Mpc^{-1}.

The *INTEGRAL* AGN sample has HX (17–60 keV) luminosities ranging over almost five orders of magnitude, from 4×10^{40} (NGC 4395) to 2×10^{45} (IGR J09446$-$2636) erg s^{-1}. Therefore, this is a representative, HX-selected sample of nearby AGNs, mostly Seyfert galaxies, although our $\sim$10 most luminous objects may be better referred to as nearby quasars because their HX luminosities exceed 10^{44} erg s^{-1}.

One special object in the sample is the Seyfert 1.8 galaxy NGC 4395, a famous LLAGN sometimes referred to as a "dwarf Seyfert nucleus." It appears to be a quite atypical Seyfert galaxy in terms of its black hole mass, luminosity, and variability properties (see, e.g., Moran et al. 1999; Peterson et al. 2005; Vaughan et al. 2005). It is therefore possible that the properties of its dusty torus (if there is any) are also different from typical Seyfert galaxies and quasars. We thus treat this object separately from the rest of the sample in performing the HX–MIR cross-correlation analysis (Section 5).

As noted above, the HX selection (17–60 keV) implies that there is almost no bias from absorption. Our AGN sample is not sensitive to photoabsorption (and we have thus not

Table 1
INTEGRAL–Spitzer AGN Sample

Name	AGN[a] Class	Reference	z	D (Mpc)	Reference	N_H[b] (10^{22} cm^{-2})	Reference	17–60 keV		15 μm		
								Flux (10^{-11} erg s^{-1} cm^{-2})	log L (erg s^{-1})	f_ν (Jy)	log νL_ν (erg s^{-1})	F_{AGN}
						Clean sample (AGN-dominated infrared sources)						
MRK 348	Sy2		0.0150	63.4		30		7.4 ± 0.8	43.55	0.413	43.60	0.97
MCG -01-05-047	Sy2		0.0172	72.8		14	6	1.6 ± 0.3	43.02	0.107	43.14	0.73
NGC 788	Sy2		0.0136	57.4		40		4.8 ± 0.3	43.28	0.216	43.23	1.00
LEDA 138501	Sy1		0.0492	213.3		<1		4.0 ± 0.7	44.33	0.029	43.50	1.00
MRK 1040	Sy1.5		0.0167	70.7		<1		4.9 ± 0.8	43.46	0.574	43.84	1.00
IGR J02343+3229	Sy2		0.0162	68.5		2	7	3.9 ± 0.6	43.34	0.128	43.16	0.73
1H 0323+342	NLSy1	1	0.0610	266.7		<1		2.7 ± 0.5	44.37	0.059	44.00	0.90
NGC 1365	Sy1.8		0.0055	17.9	5	50		3.3 ± 0.7	42.10	1.736	43.13	0.37
3C 111	Sy1, BLRG		0.0485	210.1		<1		7.8 ± 0.9	44.62	0.137	44.16	1.00
ESO 033-G002	Sy2		0.0181	76.7		1		1.9 ± 0.3	43.14	0.300	43.63	1.00
IRAS 05078+1626	Sy1.5		0.0179	75.8		<1		5.9 ± 0.8	43.61	0.471	43.81	0.96
MRK 3	Sy2		0.0135	57.0		100		6.8 ± 0.3	43.43	1.352	44.02	1.00
MRK 6	Sy1.5		0.0188	79.7		5		3.7 ± 0.3	43.45	0.361	43.74	0.96
ESO 209-G012	Sy1.5		0.0405	174.4		<1		1.7 ± 0.2	43.78	0.245	44.25	0.82
IRAS 09149−6206	Sy1		0.0573	249.8		<1		2.1 ± 0.3	44.19	0.645	44.98	1.00
MRK 110	NLSy1		0.0353	151.5		<1		5.9 ± 1.1	44.21	0.079	43.64	1.00
IGR J09446−2636	Sy1.5	2	0.1425	658.2		<1		3.9 ± 0.7	45.31	0.025	44.41	1.00
NGC 2992	Sy2		0.0077	30.5	4	1		5.1 ± 0.4	42.75	0.627	43.15	0.48
MCG -5-23-16	Sy2		0.0085	35.7		2		9.8 ± 0.8	43.17	1.111	43.53	1.00
NGC 3081	Sy2		0.0080	32.5	4	50		4.6 ± 0.6	42.77	0.490	43.09	0.96
ESO 263-G013	Sy2		0.0333	142.7		40		2.2 ± 0.4	43.72	0.086	43.62	1.00
NGC 3227	Sy1.5		0.0039	20.6	4	<1		9.1 ± 0.8	42.66	0.697	42.85	0.63
NGC 3281	Sy2		0.0107	45.1		150		3.9 ± 0.6	42.98	1.327	43.81	1.00
IGR J10386−4947	Sy1.5		0.0600	262.1		1		1.5 ± 0.2	44.08	0.081	44.12	1.00
IGR J10404−4625	Sy2		0.0239	101.7		3		2.1 ± 0.3	43.42	0.171	43.63	0.91
NGC 3783	Sy1		0.0097	38.5	4	<1		12.3 ± 1.9	43.34	1.037	43.57	1.00
IGR J12026−5349	Sy2		0.0280	119.5		2		2.4 ± 0.3	43.62	0.439	44.18	0.92
NGC 4151	Sy1.5		0.0033	20.3	4	8		47.4 ± 0.4	43.37	2.804	43.44	1.00
MRK 50	Sy1		0.0234	99.5		<1		1.3 ± 0.2	43.19	0.026	42.80	1.00
NGC 4388	Sy2		0.0084	16.8	4	40		17.9 ± 0.3	42.78	0.776	42.72	0.93
NGC 4395	Sy1.8		0.0011	4.6	5	2		1.6 ± 0.3	40.59	0.013	39.83	0.86
NGC 4507	Sy2		0.0118	49.7		60		10.9 ± 0.5	43.51	0.859	43.71	0.95
NGC 4593	Sy1		0.0090	39.5	4	<1		5.9 ± 0.3	43.04	0.477	43.25	0.78
ESO 323-G077	Sy1.2		0.0150	63.4		30		2.8 ± 0.3	43.13	0.689	43.82	0.78
IGR J13091+1137	XBONG		0.0251	106.9		90		3.5 ± 0.4	43.68	0.092	43.40	1.00
IGR J13149+4422	Sy2		0.0366	157.2		5	7	2.2 ± 0.4	43.81	0.207	44.09	0.98
Cen A	Sy2, NLRG		0.0018	3.6	5	11		56.0 ± 0.3	41.94	2.184	41.83	0.94
MCG -6-30-15	Sy1.2		0.0077	32.4		<1		3.6 ± 0.4	42.66	0.483	43.09	1.00
MRK 268	Sy2		0.0399	171.8		30	8	1.7 ± 0.3	43.79	0.127	43.95	0.84
IC 4329A	Sy1.2		0.0160	67.7		<1		16.1 ± 0.5	43.95	1.517	44.22	1.00
NGC 5506	Sy1.9		0.0062	28.7	4	3		13.3 ± 0.7	43.12	1.739	43.54	1.00
IGR J14552−5133	NLSy1		0.0160	67.7		<1		1.4 ± 0.2	42.89	0.173	43.28	0.95
IC 4518A	Sy2		0.0157	66.4		10		2.4 ± 0.2	43.11	0.410	43.64	0.87
WKK 6092	Sy1		0.0156	65.9		<1		1.7 ± 0.2	42.94	0.068	42.85	1.00
IGR J16185−5928	Sy1		0.0350	150.1		<1	9	1.7 ± 0.2	43.67	0.035	43.28	1.00
ESO 137-G034	Sy2		0.0092	38.7		≳100	10	1.7 ± 0.2	42.48	0.231	42.92	0.95
IGR J16482−3036	Sy1		0.0313	133.9		<1		2.6 ± 0.2	43.75	0.039	43.22	1.00
NGC 6221	Sy2		0.0050	19.4	4	1		1.9 ± 0.3	41.93	0.875	42.90	0.46
IGR J16558−5203	Sy1.2		0.0540	234.9		<1		2.9 ± 0.2	44.29	0.212	44.45	0.91
NGC 6300	Sy2		0.0037	14.3	4	25		4.7 ± 0.4	42.06	0.891	42.64	0.94
IGR J17418−1212	Sy1		0.0372	159.8		<1		2.6 ± 0.3	43.89	0.173	44.03	0.94
3C 390.3	Sy1, BLRG		0.0561	244.4		<1		6.2 ± 0.6	44.64	0.147	44.32	1.00
IGR J18559+1535	Sy1		0.0838	372.3		<1		2.3 ± 0.2	44.58	0.096	44.50	1.00[c]
1H 1934−063	NLSy1	3	0.0106	44.6		<1		1.8 ± 0.3	42.63	0.514	43.39	0.94
NGC 6814	Sy1.5		0.0052	22.8	4	<1		4.7 ± 0.4	42.47	0.178	42.35	1.00
Cyg A	Sy2, NLRG		0.0561	244.4		20		5.8 ± 0.3	44.62	0.323	44.67	1.00
MRK 509	Sy1.2		0.0344	147.5		<1		5.5 ± 0.8	44.16	0.395	44.31	0.89
NGC 7172	Sy2		0.0087	33.9	4	13		6.0 ± 0.5	42.92	0.349	42.98	0.65
MR 2251−178	Sy1		0.0640	280.4		<1		4.8 ± 0.5	44.65	0.119	44.35	1.00
NGC 7469	Sy1.2		0.0163	68.9		<1		4.7 ± 0.8	43.43	1.552	44.25	0.54
MRK 926	Sy1.5		0.0469	203.0		<1		3.6 ± 0.5	44.25	0.139	44.14	1.00

<div align="center">

Table 1
(Continued)

</div>

Name	AGN[a] Class	Reference	z	D (Mpc)	Reference	N_H[b] (10^{22} cm^{-2})	Reference	17–60 keV		15 μm		
								Flux (10^{-11} erg s^{-1} cm^{-2})	log L (erg s^{-1})	f_ν (Jy)	log νL_ν (erg s^{-1})	F_{AGN}
Starburst-dominated infrared sources												
NGC 1142	Sy2		0.0288	123.0		45		4.6 ± 0.4	43.92	0.065	43.37	$\lesssim 0.5$
ESO 005−G004	Sy2		0.0062	22.4	4	100	11	2.5 ± 0.5	42.18	0.196	42.37	$\lesssim 0.5$
IGR J07563−4137	Sy2		0.0210	89.1		<1		1.2 ± 0.2	43.07	0.046	42.95	$\lesssim 0.5$
NGC 4945	Sy2		0.0019	3.8	5	200		19.9 ± 0.4	41.54	1.872	41.81	$\lesssim 0.5$
IGR J14561−3738	Sy2		0.0246	104.7		$\gtrsim 100$	12	1.4 ± 0.3	43.27	0.051	43.13	$\lesssim 0.5$
MCG +04-48-002	Sy2		0.0142	60.0		50		3.3 ± 0.6	43.16	0.268	43.37	$\lesssim 0.5$
Compton-thick objects												
NGC 1068	Sy2		0.0038	14.4	4	$\gtrsim 1000$		1.9 ± 0.3	41.67	15[d]	43.87	1.00

Notes.
[a] AGN optical/radio classes are from Sazonov et al. (2007) unless a reference is given: Sy1–Sy2, Seyfert galaxy; NLSy1, narrow-line Seyfert 1 galaxy; BLRG, broad-line radio galaxy; NLRG, narrow-line radio galaxy; XBONG, X-ray-bright optically normal galaxy. The LLAGN NGC 4395 is marked in bold.
[b] X-ray absorption columns are from Sazonov et al. (2007) unless a reference is given.
[c] Poor IRS SL ($\lambda < 14\,\mu$m) data due to inaccurate slit position; spectral shape at $\lambda > 14\,\mu$m indicates negligible starburst contribution.
[d] The source is saturated in low-resolution IRS data, the flux density is from Mason et al. (2006), and AGN fraction is assumed to be 100%.
References. (1) object also exhibits some blazar properties (Zhou et al. 2007); (2) Masetti et al. 2008; (3) Rodríguez-Ardila et al. 2000; (4) Tully 1988; (5) Tully et al. 2009; (6) Landi et al. 2007; (7) Rodriguez et al. 2008; (8) *XMM-Newton* data; (9) Malizia et al. 2008; (10) Malizia et al. 2009; (11) Ueda et al. 2007; (12) Sazonov et al. 2008a.

corrected the measured HX fluxes for line-of-sight absorption) as long as the column density of the gas is less than a few 10^{24} cm^{-2} or equivalently the Thomson optical depth is less than a few; at even larger column densities, the flux from a source drops considerably at all X-ray energies. The Seyfert 2 galaxy NGC 1068 distinguishes itself from the rest of the sample because it is the only significantly Compton-thick AGN (having $N_H \gtrsim 10^{25}$ cm^{-2}; Matt et al. 2000). We therefore exclude NGC 1068 from our baseline HX–MIR cross-correlation analysis but discuss its properties in comparison with Compton-thin sources (Sections 5 and 6).

3. *SPITZER* OBSERVATIONS AND DATA REDUCTION

More than half of the *INTEGRAL* sample consists of well-known Seyfert galaxies, many of which have been targets of observational campaigns with *Spitzer*. For the remaining part, largely represented by AGNs discovered by *INTEGRAL*, we carried out short *Spitzer* observations (Program ID 50763) consisting of 3.6–8 μm imaging with InfraRed Array Camera (IRAC) and low-resolution MIR spectroscopy with InfraRed Spectrograph (IRS); in addition, far-infrared photometry was performed with MIPS for a subset of objects. Our proprietary and publicly available archival data together provide complete coverage of the *INTEGRAL* sample with *Spitzer* at 3.6–38 μm.

All of the sources in our HX-selected sample would have been robustly detected by *Spitzer* even if they had been 1–3 orders of magnitude fainter. Hence, our sample is not limited by MIR flux and any correlations derived between the HX and MIR luminosities can be considered representative of the local AGN population without significant bias.

3.1. IRS

We used the IRS (Houck et al. 2004) on *Spitzer* to obtain low-resolution spectra of our objects. Our program's observations, for a total of 30 AGNs, were done in spectral mapping mode using the short–low (SL) and long–low (LL) IRS modules. Each

of these modules has first- and second-order sub-slits (SL1, SL2, LL1, and LL2) with widths of 3.7, 3.6, 10.7, and 10.5 arcsec, respectively. We used SL1, LL1, and LL2 for the entire sample and SL2 for a subset of objects. The resulting spectra thus cover a range from either 5.2 or 7.5 μm up to 38 μm. Observations with SL1 and SL2 consisted of one cycle of six pointings with a ramp duration of 6 s with two 19″ steps in the slit direction and three 1″.8 steps in the dispersion direction. For LL1 and LL2, one cycle of three pointings with a ramp duration of 6 s and a step size of 42″ in the slit direction was implemented.

For those sources that were not covered by our *Spitzer* program, we used archival low-resolution IRS data: mapping mode observations for 14 AGNs and staring mode observations for another 23 AGNs. Almost all of the archival mapping mode observations have the following setup: one cycle of 13 pointings with a step size of 1″.8 in the dispersion direction for SL1 and SL2 and 5 pointings with a step size of 4″.85 in the dispersion direction for LL1 and LL2, the ramp duration being 6 s. For the archival staring mode observations, the ramp times and numbers of cycles vary from one object to another.

In the analysis of mapping mode observations, we used basic calibrated data (BCD), extracted from the Spitzer Science Center pipeline (versions S18.0.1 and newer for our program's observations and versions S15.3.0 and newer for the archival observations). For each order of a given IRS module and for each position of a given source within the slit, we first produced a background image. For our program's observations, this was done by averaging over two-dimensional (2D) spectra obtained in significantly (~19″ for SL and ~42″ for LL) off-source positions, whereas for the archival observations, a similar averaging was done over 2D spectra obtained in the other order of a given IRS module. The background image was then subtracted from the on-source 2D spectrum. Then, a 1D spectrum of the source was obtained using the Spitzer IRS Custom Extraction (SPICE) software by applying the regular extraction algorithm, which uses an aperture that gradually increases with wavelength in accordance with the telescope's

point-spread function (e.g., the aperture width is 7.″2 at 6 μm and 36.″6 at 27 μm). Finally, an averaging over a set of 1D spectra extracted in different source positions within the slit was done. The staring mode spectra were obtained simply by averaging over nod-subtracted post-BCD spectra. These were derived with the same regular extraction algorithm as was used in our analysis of mapping mode observations.

Although the data reduction procedure described above is fairly simplistic and does not fully exploit the potential of mapping mode observations (which are available for nearly two-thirds of our sample), it is adequate for the purposes of our HX–MIR cross-correlation study, as confirmed by a comparison with an alternative, more detailed analysis of IRS data for a subset of *INTEGRAL* sources (see Section 4.4).

The Compton-thick Seyfert 2 galaxy NGC 1068 is an extremely bright (∼15 Jy at 15 μm) infrared source, which caused saturation of IRS. We therefore quote in Table 1 its MIR flux estimate based on a compilation of high angular resolution, infrared observations (Mason et al. 2006).

3.2. IRAC

We used images obtained by the IRAC (Fazio et al. 2004) to determine source flux densities at 3.6, 4.5, 5.8, and 8.0 μm. This wavelength range partially overlaps with that covered by IRS spectroscopy, enabling direct comparison between the spectroscopic and photometric results and providing an extension of spectra to shorter wavelengths.

Our IRAC program included 35 *INTEGRAL* sources. Observations were done in high dynamic range (HDR) mode. Specifically, a combination of a 0.6 s frame and a 12 s frame was repeated in nine random dithers for each source. For the rest of the sample, we made use of archival observations for which the number and duration of frames varied from source to source. Since most of our objects are bright infrared sources, our analysis was in most cases based on stacking the 0.6 s frames. For the five weakest sources (≲10 mJy at 3.6–8.0 μm), including LEDA 138501, IGR J09446−2636, ESO 263-G013, IGR J10386−4947, and NGC 4395, to improve the accuracy, we determined the fluxes by stacking the long (2, 12, or 30 s) frames. This was also done for 3C 111 and Mrk 3 despite their relative brightness because the observations were not done in HDR mode. We verified that none of the sources were saturated.

We analyzed post-BCD data using the standard point-source extraction package APEX, part of the MOPEX software. Post-BCD images are adequate for this work because their main deficiency, poor artifact correction, is unimportant for 0.6 s frames. We estimated source fluxes by integrating the surface brightness in different apertures with radii between 2.″4 and 12″ and correcting for flux leakage outside the aperture under the assumption of a point-like source. Although this procedure is inaccurate for measuring fluxes of spatially extended sources, it is good enough to indicate the presence of extended host galaxy emission as a significant difference between fluxes measured in large and small apertures (see Appendix A).

The existing IRAC photometric measurements for the Compton-thick Seyfert 2 galaxy NGC 1068 proved to be saturated and hence were not used.

4. INFRARED SPECTRA: AGN MIR EMISSION

Infrared emission from dust associated with star formation in the host galaxy can provide a significant contribution to AGN MIR spectra. Therefore, to study torus emission, we need to estimate and subtract the star formation contribution from the *Spitzer* data. We observe clear signatures of star formation in many of our IRS spectra. These include polycyclic aromatic hydrocarbon (PAH) emission features and the νF_ν continuum rising toward the far-infrared. We therefore modeled the measured spectra by a sum of starburst and AGN components, similarly to a number of previous studies (e.g., Netzer et al. 2007; Mullaney et al. 2011).

Figure 1 shows examples of IRS spectra with negligible, significant, and strong star formation contribution as deduced using the fitting procedure described below. At short wavelengths, we also show IRAC photometric fluxes measured in 2.″4 and 12″ apertures.

4.1. Spectral Decomposition Using a Starburst Template

We adopted the starburst template from Brandl et al. (2006),[8] which is an average over low-resolution IRS spectra of a dozen nearby (D ≲ 100 Mpc) starburst galaxies. This template is well suited for our analysis because it was obtained by low-resolution IRS spectroscopy, similarly to the spectra studied here.

We normalized starburst components in our objects based on the observed strength of PAH lines, which are believed to be a generic signature of star formation (Roche et al. 1991). The presence of an AGN in a star-forming galaxy may lead to a weakening of the PAH spectral features because PAH molecules can be destroyed by hard AGN radiation (Voit 1992). However, the importance of this effect is controversial (see, e.g., Smith et al. 2007b; O'Dowd et al. 2009; Sales et al. 2010), and we have assumed that the shape of the starburst spectral component is not affected by the presence of a central AGN.

Our analysis consisted of the following steps. First, we fitted the spectra around (typically within ±0.6 μm of) the 6.2 μm and 11.3 μm PAH lines by a sum of a linear continuum and a Gaussian. We then compared the derived PAH line fluxes with the corresponding values for the starburst template, which yielded two independent estimates of the amplitude of the star-formation component. The average of these two values was then adopted as the normalization of the starburst template. On average, the coefficients implied by the 6.2 μm and 11.3 μm features proved to be consistent with each other, although there is ∼40% scatter around the 1:1 ratio of the two coefficients. This indicates that there are ∼20% systematic uncertainties in the derived amplitudes of starburst components for our objects (this issue is further discussed in Section 4.4 below). If there were no IRS data for the 6.2 μm feature (i.e., only first-order SL data at ≳7.5 μm were available), we used the flux of the 11.3 μm line to normalize the starburst component. If the observed PAH features proved to be strong enough (depending on the source brightness, we required the PAH equivalent widths, EW, to be larger than 0.01–0.02 μm, as compared to EW = 0.45 and 0.55 μm for the 6.2 μm and 11.3 μm bands, respectively, in the starburst template), we subtracted the estimated starburst contribution from the total spectrum to derive the AGN component. Otherwise, we considered star formation contamination insignificant and did not perform any subtraction.

We applied an additional correction to 13 spectra that contained detectable PAH features and exhibited a significant (>10%–20%, depending on the source brightness) discontinuity near 14 μm, where the short-wavelength segment measured in the 3.″7-wide SL1 slit connects to the long-wavelength segment measured in the 10.″5-wide LL2 slit. Such a "jump" is most

---

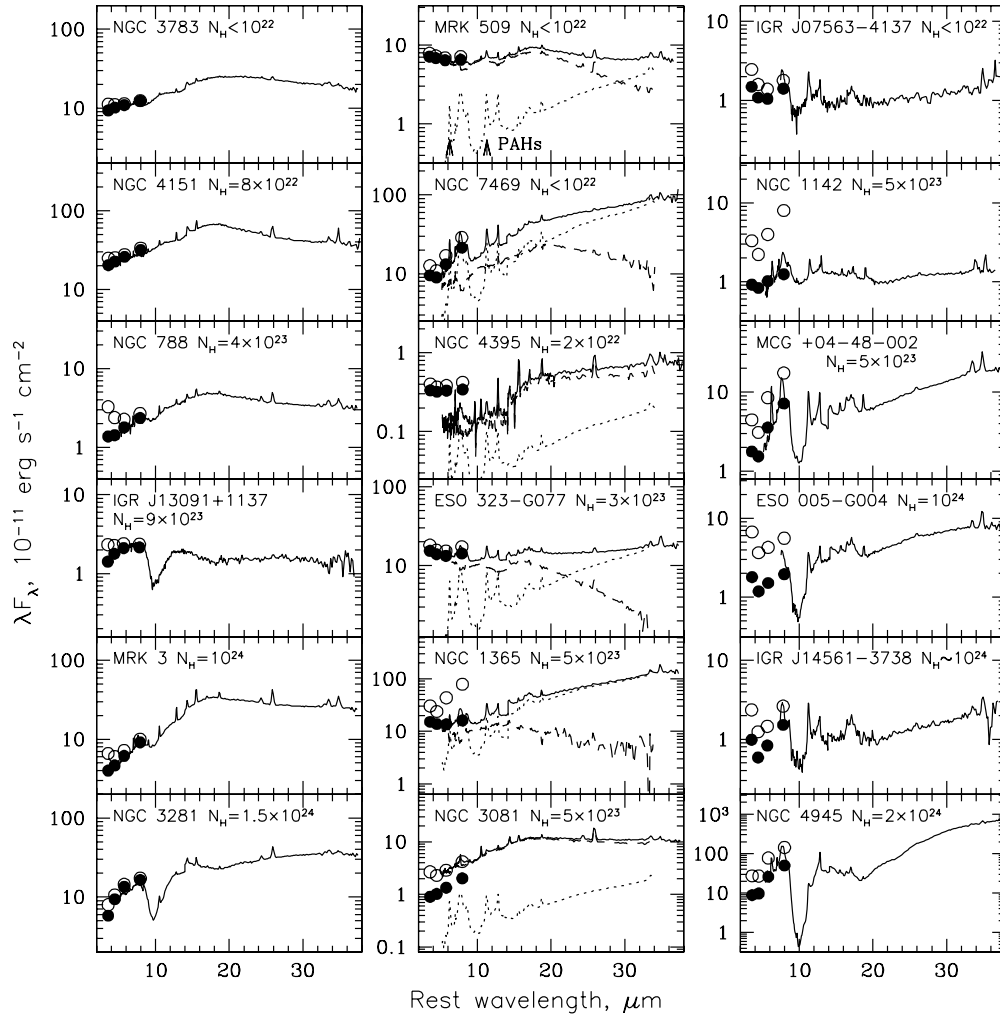[8] http://www.strw.leidenuniv.nl/~brandl/SB_template.html

Figure 1. Examples of *Spitzer* spectra of *INTEGRAL* AGNs. In each panel, the solid line shows the low-resolution IRS spectrum, and the filled and open circles represent fluxes at 3.6, 4.5, 5.8, and 8.0 μm derived from IRAC images in 2″.4 and 12″ apertures, respectively (corrected for flux leakage outside the aperture assuming a point source). Also, the X-ray absorption columns are indicated. Left column: spectra that are clearly dominated by dust emission associated with the active nucleus, with a weak or absent starburst contribution. Middle column: spectra showing a noticeable contribution of MIR emission from dust associated with star formation. The dotted line shows the starburst component, estimated by fitting the starburst template to the 6.2 and 11.3 μm PAH lines (indicated in the upper panel). The dashed line shows the AGN contribution, found as the difference between the total spectrum and the starburst component; it may still be contaminated at short wavelengths by stellar and accretion disk emission. Right column: starburst-dominated spectra for which extraction of an AGN component is practically impossible. Note the much broader flux range covered by the spectrum of NGC 4945 compared to the other sources.

likely caused by an extended source, i.e., it cannot be due to the AGN. In these objects, the long-wavelength ($\gtrsim 14\,\mu$m) part of the starburst component was rescaled to make the AGN component smooth across the SL–LL boundary. We did not make such a correction for NGC 4395, by far the weakest infrared source in our sample (with an estimated flux density of 13 mJy at 15 μm), despite the apparent presence of a significant SL–LL discontinuity in its spectrum, because of its low statistical quality (see Figure 1). Furthermore, our comparison with available high-resolution spectroscopy for this object (see Section 4.2 below) indicates that the SL slit was not positioned sufficiently accurately on the nucleus of NGC 4395, which might have caused an artificial discontinuity at 14 μm in the low-resolution IRS spectrum.

In principle, we could also use another known strong PAH feature, at 7.7 μm, for estimating the contribution of star formation. However, this band overlaps with the high-ionization [Ne VI] 7.65 μm line, which can be bright in AGNs (Sturm et al. 2002) and is impossible to separate from the PAH feature in low-resolution IRS spectra. Moreover, the 7.7 μm feature might

be significantly affected by AGN radiation (Smith et al. 2007b; O'Dowd et al. 2009).

4.2. AGN-dominated (Clean Sample) versus Starburst-dominated Sources

In agreement with previous studies (e.g., Weedman et al. 2005; Buchanan et al. 2006; Shi et al. 2006; Deo et al. 2009; Wu et al. 2009), we observe a large variety of infrared spectral shapes among Seyfert galaxies. However, those spectra dominated by dust-reprocessed emission generated by black hole accretion (see examples in the left column of Figure 1), rather than by star formation, almost invariably peak (when plotted in νF_ν units) at ~15–20 μm, in good agreement with models of dusty tori heated by a central source of UV radiation (e.g., Dullemond & van Bemmel 2005; Hönig et al. 2006; Nenkova et al. 2008; Alonso-Herrero et al. 2011). Furthermore, the AGN components of those IRS spectra with inferred significant starburst contamination (see the middle column of Figure 1) prove to be similar to the spectra of "pure" AGNs. In particular, most of the former also peak at 15–20 μm. However, since our procedure of estimating

the star formation contribution based on the strength of PAH features becomes progressively less reliable with increasing wavelength, there is much uncertainty in the deduced AGN spectral contributions at $\lambda \gtrsim 20\,\mu$m. All these findings are similar to the results of previous attempts to decompose *Spitzer* spectra of quasars and Seyfert galaxies into AGN and starburst components (e.g., Netzer et al. 2007; Mullaney et al. 2011).

The IRS spectra of six objects, NGC 1142, ESO 005-G004, IGR J07563−4137, NGC 4945, IGR J14561−3738, and MCG+04-48-002 (see the right column of panels in Figure 1), closely resemble the starburst template. We found it practically impossible to distinguish AGN and host galaxy components in these starburst-dominated sources and therefore excluded them (see Table 1) from most of the subsequent analysis. Interestingly, most of our starburst-dominated objects are strongly X-ray-absorbed AGNs ($N_{\rm H} \sim 10^{24}$ cm^{-2}). One may speculate that (1) large supplies of cold gas and dust associated with starburst activity in a galactic nucleus facilitate the formation of a dense central obscuring torus, and/or (2) part of the X-ray absorption is caused by cold gas tracing star formation in the galaxy and located outside a parsec-scale AGN torus.

The remaining 61 objects (with NGC 1068 excluded for being a Compton-thick source) compose a "clean" sample for our subsequent analysis. As concerns the LLAGN NGC 4395, since its (low signal-to-noise) low-resolution IRS spectrum leaves doubts as to the presence of a significant starburst contribution (we estimate it at ∼14% at 15 μm), we have also analyzed available high-resolution IRS data, following the methods described by Goulding & Alexander (2009). While the derivation of an accurate continuum shape, using only high-resolution IRS, is complicated by the tip-tilt effects of the individual echelle orders, the high-resolution MIR spectrum of NGC 4395 is characterized almost entirely by an AGN-produced broken power law with little or no evidence (EW $\ll 0.1\,\mu$m) for superposed PAH features. Hence, NGC 4395 is clearly AGN dominated and thus should be part of our clean sample. Nevertheless, as noted before, we still distinguish this "dwarf Seyfert" from the rest of the sample during our HX–MIR cross-correlation analysis because it might represent a physically different class of AGNs.

4.3. 15 μm Flux and Luminosity

We have just seen (Figure 1 and Section 4.2) that after subtraction of the star formation contribution, AGN MIR continua have an approximately constant shape. This suggests that it should be possible to estimate bolometric luminosities of AGN obscuring tori using their flux densities measured at a single MIR wavelength. We have chosen to use for this purpose the rest-frame $\lambda = 15\,\mu$m. Specifically, f_ν (15 μm) was determined by averaging a given spectrum over the wavelength range 14.7–15.2 μm. There are several reasons behind this choice. First, $\lambda = 15\,\mu$m is approximately where AGN torus emission peaks. Second, since IRS SL2 data are not available for some of our sources, we can only use wavelengths $\lambda \gtrsim 8\,\mu$m for the whole sample. Third, wavelengths $\lambda \gtrsim 20\,\mu$m are disfavored because cool dust emission associated with star formation becomes more important with increasing wavelength and frequently dominates far-infrared and even MIR spectra of Seyferts. Finally, there are no strong emission lines or absorption features within ∼0.5 μm on either side of 15 μm.

The last three columns of Table 1 present the total measured flux densities (f_ν) and corresponding luminosities (νL_ν) at 15 μm, as well as estimated fractions of AGN emission in

the total flux at 15 μm, $F_{\rm AGN}$. Statistical uncertainties for the infrared fluxes and luminosities are negligibly small. For the six starburst-dominated objects, we assume that $F_{\rm AGN} \lesssim 50\%$. In the subsequent analysis, the starburst-subtracted MIR flux of AGNs is defined as

$$f_{15\,\mu\rm m} = F_{\rm AGN}\nu f_\nu(15\ \mu\rm m). \qquad (1)$$

The corresponding AGN luminosity is defined as

$$L_{15\,\mu\rm m} = F_{\rm AGN}\nu L_\nu(15\ \mu\rm m). \qquad (2)$$

4.4. Uncertainty in AGN MIR Flux Estimates

The main potential source of systematic uncertainty in our estimation of AGN fluxes at 15 μm is the use of a fixed starburst spectral template from Brandl et al. (2006). In reality, the spectral properties of infrared emission from dust heated by starbursts may vary from one galaxy to another, and some authors (e.g., Mullaney et al. 2011) have attempted to take this diversity into account in separating AGN and host galaxy components for Seyfert galaxies.

A crude estimate of the systematic uncertainty associated with our use of a fixed spectral template was already made in Section 4.1 using the difference in the normalizations of starburst spectral components determined using the 6.2 and 11.3 μm PAH features. Namely, starburst component amplitudes could be estimated by our fitting procedure to within ∼20%. This implies that for AGN-dominated sources, i.e., those objects with $F_{\rm AGN} \gtrsim 50\%$, the AGN fluxes at 15 μm are also estimated to within ∼20%, i.e., to better than 0.1 dex in log space.

To better understand the uncertainties associated with our estimates of $f_{15\,\mu\rm m}$, we performed an alternative spectral analysis based on a set of starburst spectral templates for a subsample of our objects. Specifically, we selected a representative subset (16 objects) of AGN-dominated, mixed, and starburst-dominated sources. This comparison sample is equally divided between sources with IRS-staring and mapping data. In Section 4.1, we assumed that the SL–LL discontinuity observed in the MIR spectra of some of these AGNs arises due to extended host galaxy emission, which provides an additional contribution to the larger aperture LL spectrum. However, it has also been suggested in previous studies that this discontinuity between the spectral orders derives from an IRS detector effect; for the purposes of comparison, we imposed this assumption for our subsample. Furthermore, for those sources with IRS mapping data, we combined the rogue-pixel cleaned BCD images and extracted nuclear spectra using the 3D spectral reduction program CUBISM (Smith et al. 2007a), which is used widely in recent MIR AGN literature (e.g., Dale et al. 2009; Goulding & Alexander 2009; Diamond-Stanic & Rieke 2010; Petric et al. 2011; Alonso-Herrero et al. 2012). We used DecompIR (Mullaney et al. 2010) to deconvolve the MIR spectra for our comparison sample using a set of empirical and theoretical starburst templates (e.g., Goulding et al. 2011) and assumed an absorbed broken power law to model the AGN component. The derived AGN fractions and fluxes prove to be entirely consistent with the values established by our baseline analysis (Sections 3.1 and 4.1) for those sources with $F_{\rm AGN} > 0.5$ (the average scatter in the derived $f_{15\,\mu\rm m}$ is ±8%). However, for those sources with $F_{\rm AGN} < 0.5$ (i.e., the spectra appear starburst dominated), the spectral fits become strongly dependent on the imposed starburst templates, and the scatter in the measured AGN flux increases to a factor of ∼2.

As an additional check of our IRS spectral measurements, we can use the IRAC imaging data available for all of our AGNs. For the vast majority of the sources, the absolute values of flux densities measured by IRAC and IRS in the overlapping spectral region below 8 μm are in good mutual agreement (see Figure 1), especially when the smallest (2″.4) IRAC aperture is used (recall that the IRS SL slits have similar widths, 3″.6–3″.7). However, there are a few sources for which there is a significant discrepancy between the spectroscopic and photometric fluxes at $\lambda \lesssim 8\,\mu$m. Since the corresponding IRAC and IRS observations were separated by several years in time, these flux differences probably indicate significant intrinsic variability of AGN torus emission, especially at shorter wavelengths (Suganuma et al. 2006; Kishimoto et al. 2009; Tristram et al. 2009; Kozłowski et al. 2010). Also, as shown in Appendix A, the detection of significant extended emission at 8 μm by IRAC in many sources is fully consistent with our conclusions about the host-galaxy contamination of IRS spectra.

Finally, we compared our results for 16 AGNs with higher angular resolution observations from Gandhi et al. (2009). We find excellent agreement (see Figure 5 and discussion in Section 5.2) between the fluxes derived from the very different observational data sets, which suggests that host galaxy contamination of our measured values of AGN MIR fluxes is minimal.

We conclude that the combined statistical and systematic uncertainty in our AGN 15 μm flux estimates for the clean sample (i.e., AGN-dominated sources) is probably less than 0.1 dex. This uncertainty proves to be small in comparison with the intrinsic scatter in the HX–MIR flux and luminosity correlations (see Section 5 below). We further discuss the potential influence of starburst contamination on our derived correlations in Section 5.1.

5. HX–MIR LUMINOSITY RELATION

Before comparing the luminosities of AGN structural components (accretion disk, corona, and obscuring torus), which will be the subject of Section 6, we first perform a cross-correlation analysis of AGN luminosities measured in the HX and MIR bands by *INTEGRAL* and *Spitzer*, respectively. The results of this analysis may also be interesting in their own right for any studies addressing links between X-ray and infrared emission in AGNs.

Figure 2 shows the scatter plot of $L_{15\,\mu m}$ versus L_{HX}, where L_{HX} is the luminosity in the 17–60 keV energy band and $L_{15\,\mu m}$ was defined in Equation (2). In computing luminosities from fluxes, we neglected uncertainties associated with source distances.

Considering the clean AGN sample without NGC 4395 and fitting $L_{15\,\mu m}$ as a function of L_{HX} (computing the linear regression in log–log space), we find a strong, nonlinear correlation between MIR and HX luminosities (see Table 2):

$$L_{15\,\mu m,43} = (1.7 \pm 0.2) L_{HX,43}^{0.74 \pm 0.06}, \qquad (3)$$

where the luminosities are measured in units of 10^{43} erg s^{-1}. The rms scatter of $L_{15\,\mu m}$ values around the mean trend is 0.34 dex.

As can be seen in Figure 2, NGC 4395 is a clear outlier from the luminosity correlation, with its MIR luminosity being almost two orders of magnitude below the L_{HX}–$L_{15\,\mu m}$ trend described by Equation (3). If we consider this LLAGN together with the rest of the clean sample, the slope of the correlation increases
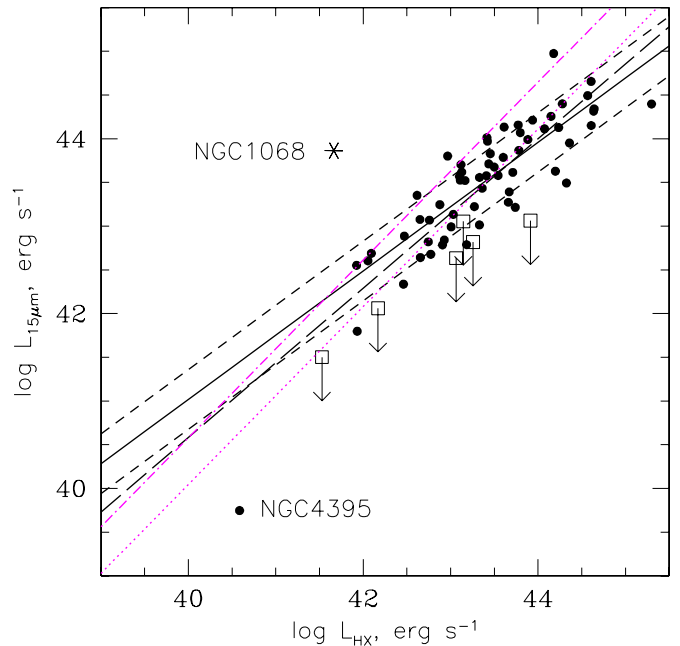

Figure 2. Luminosity scatter plot of $L_{15\,\mu m}$ vs. L_{HX}. Filled circles represent AGNs from the clean sample (excluding six starburst-dominated AGNs). The black solid line shows the best-fitting power law ($L_{15\,\mu m}$ as a function of L_{HX}) for these objects excluding NGC 4395 (Equation (3)), while the two black dashed lines show this dependence multiplied and divided by 2.19, the rms scatter around the mean trend. The black long-dashed line shows the best-fitting relation for the total clean sample including NGC 4395. The correlation parameters are listed in Table 2. Empty squares denote the six starburst-dominated sources for which an AGN fraction $F_{AGN} < 50\%$ at 15 μm is assumed. Also shown is the Compton-thick Seyfert 2 galaxy NGC 1068. The magenta dotted line shows the result of fitting L_{HX} as a function of $L_{15\,\mu m}$ by a power law, Equation (B1), for the clean sample excluding NGC 4395. The magenta dash-dotted line shows the same dependence corrected for the Malmquist bias, Equation (B2).

(A color version of this figure is available in the online journal.)

from 0.74 to 0.85 (see Table 2), although formally the change is not significant.

Figure 2 also shows the six starburst-dominated sources, assuming that their AGN fractions $F_{AGN} < 50\%$. Surprisingly, the upper limits to the 15 μm fluxes of AGN components for all these objects lie below the best-fitting relation for AGN-dominated sources (Equation (3)). At least in some cases, this behavior is likely caused by attenuation of the intrinsic MIR emission from the nucleus in the obscuring torus and in the surrounding galaxy (see Goulding et al. 2012). In particular, the IRS spectrum of NGC 4945 (Figure 1) exhibits a very deep silicate absorption trough at 10 μm, which, assuming the standard composition of interstellar dust (Draine 2003) and the simplest scenario of an infrared source surrounded by a shell of dust, suggests that the neighboring continuum emission at ~15 μm should be attenuated by a factor of ~3–5. In reality, depending on the actual distribution of dust in the nucleus and body of the galaxy, the AGN MIR emission can be absorbed even more strongly than suggested by the depth of the 10 μm trough.

Finally, Figure 2 shows the Compton-thick Seyfert 2 galaxy NGC 1068, which is a clear outlier from the correlation between L_{HX} and $L_{15\,\mu m}$ described by Equation (3). This result is expected because intrinsic HX emission is strongly absorbed in this object, and it is only the infrared signal that reveals the true power of this AGN. In fact, the discrepancy between the general trend and the position of NGC 1068 on the

Table 2
Results of HX–MIR Cross-correlation Analysis for the Clean Sample of AGNs and Its Subsamples: $L_{15\,\mu m,43} = a L_{HX,43}^{b}$

Sample	Number of Objects	a	b	rms (dex)	Spearman ρ	Spearman P_{null}	Pearson r	Pearson P_{null}
Without NGC 4395	60	1.7 ± 0.2	0.74 ± 0.06	0.34	0.85	7×10^{-18}	0.85	8×10^{-18}
All	61	1.4 ± 0.2	0.85 ± 0.06	0.39	0.86	9×10^{-19}	0.88	3×10^{-20}
$F_{AGN} \geqslant 0.9$	46	1.7 ± 0.3	0.72 ± 0.07	0.35	0.82	5×10^{-12}	0.84	5×10^{-13}
Without NGC 4395, total MIR fluxes	60	2.0 ± 0.2	0.68 ± 0.06	0.35	0.83	1.2×10^{-16}	0.82	8×10^{-16}
$z < 0.02$ (without NGC 4395)	35	1.8 ± 0.2	0.93 ± 0.10	0.29	0.84	3×10^{-10}	0.85	1.3×10^{-10}
$z > 0.02$	25	1.7 ± 0.8	0.69 ± 0.16	0.38	0.67	2×10^{-4}	0.66	3×10^{-4}
Sy1s and NLSy1s	33	2.1 ± 0.4	0.69 ± 0.09	0.37	0.81	1.2×10^{-8}	0.80	2×10^{-8}
Sy2s (without NGC 4395)	27	1.7 ± 0.2	0.85 ± 0.09	0.30	0.85	3×10^{-8}	0.88	1.7×10^{-9}
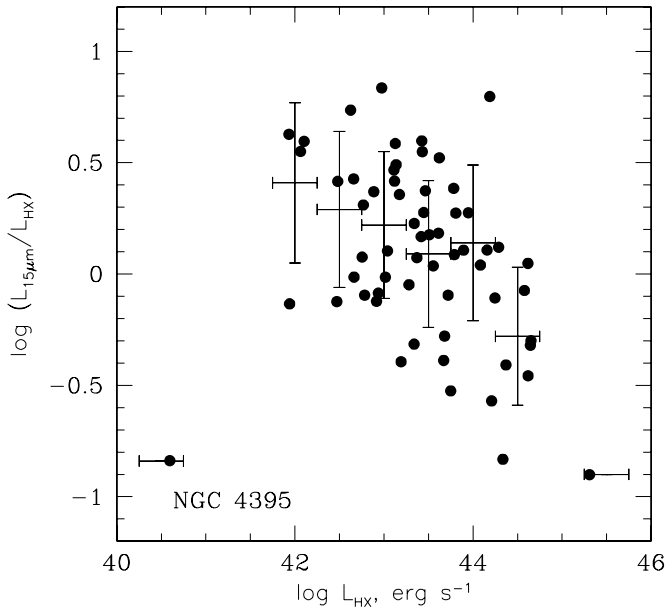
Figure 3. $L_{15\,\mu m}/L_{HX}$ ratio as a function of L_{HX} for the clean sample of AGNs. The uncertainties associated with the luminosities are less than ∼0.1 dex. Averages over 0.5 dex wide bins in L_{HX} are also shown, with the vertical error bars illustrating the rms scatter of individual measurements within bins.

$L_{HX}-L_{15\,\mu m}$ diagram suggests that its true X-ray luminosity is two orders of magnitude higher than measured by *INTEGRAL*, i.e., $L_{HX,unabsorbed} \sim 10^{44}$ erg s^{-1}. This estimate is consistent with values reported in the literature (e.g., Matt et al. 2000).

The mean trend described by Equation (3) suggests that the MIR/HX luminosity ratio decreases with increasing L_{HX}. This can be better seen in Figure 3, which shows the $L_{15\,\mu m}/L_{HX}$ ratio as a function of L_{HX}. Grouping our clean sample into 0.5 dex wide bins in L_{HX} shows that the $L_{15\,\mu m}/L_{HX}$ ratio decreases from ∼1–3 at $L_{HX} \sim 10^{42}$–10^{43} erg s^{-1} to ∼0.3–1 at $L_{HX} \sim 10^{44}$–10^{45} erg s^{-1}, although the "dwarf Seyfert" NGC 4395 is a clear outlier from this trend.

5.1. Robustness of the Correlation

The derived $L_{HX}-L_{15\,\mu m}$ relation, Equation (3), makes it possible to predict the HX luminosity for a given MIR luminosity. The combination of three facts, (1) that our AGN sample is HX selected, (2) that this sample is not limited by sensitivity in the MIR band, and (3) that the correlation has been derived by fitting $L_{15\,\mu m}$ as a function of L_{HX}, ensures that this relation reproduces the intrinsic correlation between L_{HX} and $L_{15\,\mu m}$ for the local AGN population without any bias.

To further test the robustness of the derived trend, we repeated our $L_{HX}-L_{15\,\mu m}$ cross-correlation analysis for various subsamples of AGNs. First, one may ask whether our procedure of separating AGN and starburst spectral components significantly affects the results. To address this issue, we computed the correlation for 46 strongly AGN-dominated sources—those objects in which the AGN component accounts for at least 90% of the total emission at $15\,\mu m$ (i.e., $F_{AGN} > 0.9$). The result (see Table 2) is very close to the correlation found for the total clean sample from which NGC 4395 is excluded (Equation (3)). In addition, we repeated the analysis for the clean sample (without NGC 4395) using total measured $15\,\mu m$ fluxes instead of AGN fluxes (i.e., setting $F_{AGN} = 1$). The amplitude of the correlation increased by ∼20%, obviously due to the unsubtracted contribution of starburst emission, but the slope changed by less than 1σ from 0.74 to 0.68. These tests demonstrate that the correlation between L_{HX} and $L_{15\,\mu m}$ is not significantly affected by the details of our spectral analysis of IRS data.

We next repeated the analysis separately for nearby ($z < 0.02$, 35 objects, excluding NGC 4395) and distant ($z > 0.02$, 25 objects) sources from the clean sample. The correlation, in particular the slope of 0.69 ± 0.16, derived for the distant subsample (see Table 2) is fully consistent with the correlation found for the total sample (Equation (3)). Since the $z > 0.02$ set, owing to the *INTEGRAL* detection limit, is represented by luminous AGNs only, with $L_{HX} \sim 10^{43}$–10^{45} erg s^{-1}, this result also implies that the slope of the high-luminosity part of the HR–MIR correlation is not significantly different from the trend found over a broader range of luminosities. However, the slope, 0.93 ± 0.10, determined for the nearby ($z < 0.02$) subsample, mainly consisting of lower luminosity AGNs with $L_{HX} \sim 10^{42}$–10^{44} erg s^{-1}, is somewhat different from the general trend, but this difference is less than 2σ significant.

Finally, we repeated our analysis for different types of AGNs, namely, Seyfert 1s (Sy1, including the intermediate types 1.2 and 1.5) and Seyfert 2s (Sy2, including the intermediate types 1.8 and 1.9). The derived relations (Table 2) are consistent with each other and with Equation (3). As can be seen from Figure 4, Sy1s and Sy2s do not distinguish themselves on the $L_{HX}-L_{15\,\mu m}$ diagram, nor do narrow-line Seyfert 1 galaxies occupy a distinct region of this diagram. Finally, there is no significant dependence of the $L_{15\,\mu m}/L_{HX}$ ratio on the X-ray absorption column density except for the clear separation of the extremely Compton-thick source NGC 1068 from the rest of the sample.

We conclude that the correlation between HX and MIR luminosities described by Equation (3) is robust, although there is a weak indication that the slope of the correlation is not constant and decreases with increasing AGN luminosity.
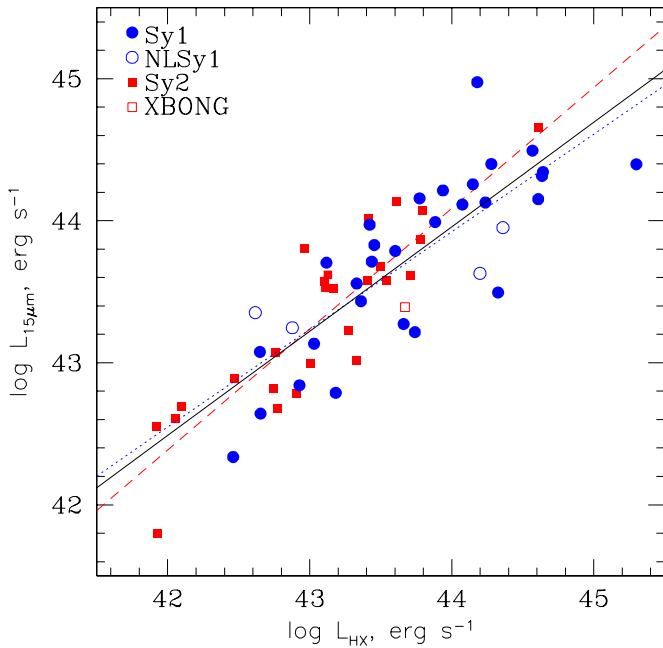
9

Figure 4. Scatter plot of $L_{15\,\mu m}$ vs. L_{HX} for the clean sample of AGNs excluding NGC 4395. Blue filled circles and red squares denote Seyfert 1s and Seyfert 2s, respectively. Also indicated are narrow-line Seyfert 1s (empty circles) and the X-ray-bright optically normal galaxy IGR J13091+1137 (empty square). The solid black, dotted blue, and dashed red lines show the best-fitting power laws for the clean sample (without NGC 4395), Sy1s, and Sy2s, respectively (Table 2).

(A color version of this figure is available in the online journal.)

For some applications, one may also be interested in knowing the distribution of L_{HX} for a given $L_{15\,\mu m}$, rather than $L_{15\,\mu m}$ as a function of L_{HX}. We have therefore also computed (Appendix B) the inverse linear regression, i.e., $\log L_{HX}$ as a function of $\log L_{15\,\mu m}$, for our clean sample excluding NGC 4395. As can be seen in Figure 2, this relation is different from the dependence of $L_{15\,\mu m}$ on L_{HX}.

5.2. Comparison with Previous Work

Mullaney et al. (2011) have studied infrared properties of nearby AGNs detected in the 14–195 keV energy band by *Swift*/BAT. This sample, although not statistically complete, is similar to our *INTEGRAL* sample in that it is HX selected. Using a subsample of AGNs having both *Spitzer*/IRS spectroscopic and *IRAS* photometric data, Mullaney et al. (2011) developed and tested a procedure, based on a set of starburst spectral templates, that makes it possible to separate AGN and starburst contributions to the infrared flux using *IRAS* four-band photometry only. They then applied this procedure to a sample of 44 BAT AGNs and found that $L_{12\,\mu m,43} = (2.4 \pm 0.4)L_{14-195\,keV,43}^{0.74\pm0.13}$. This result is in excellent agreement with our Equation (3).

On the other hand, Gandhi et al. (2009) have reported a near proportionality between 2–10 keV (L_X) and 12 μm luminosities for Seyfert galaxies using high angular resolution infrared observations: their best estimate is $L_{12\,\mu m} \propto L_X^{1.11\pm0.07}$. This result seems to contradict our conclusion that the $L_{15\,\mu m}/L_{HX}$ ratio decreases with increasing luminosity.

A number of factors might contribute to this discrepancy, but the most important one appears to be the difference in sample luminosities. A difference in galaxy weighting makes at most a minor difference. In their preferred regression procedure, Gandhi et al. (2009) took into account individual uncertainties
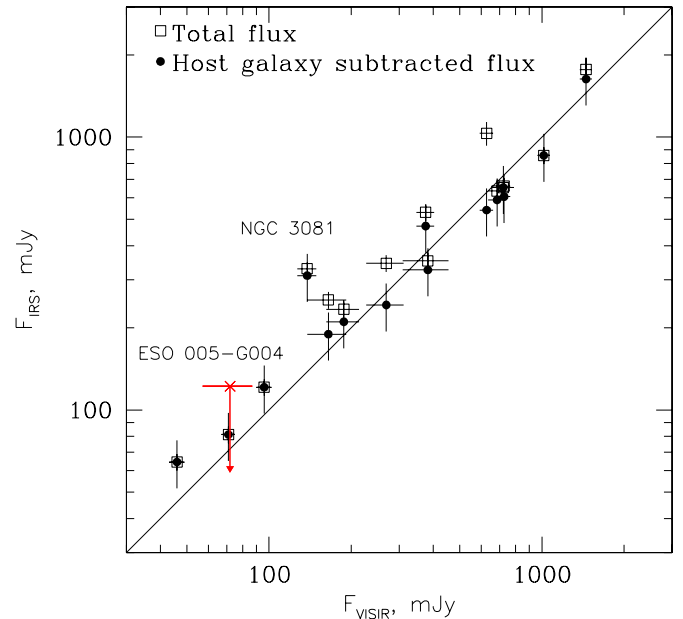

Figure 5. Comparison of fluxes measured at $\lambda \approx 12\,\mu$m by VLT/VISIR (Gandhi et al. 2009) and *Spitzer*/IRS. The black empty squares are total IRS fluxes, and the black dots are starburst-subtracted fluxes, to which systematic uncertainties of 20% are ascribed. The red cross with the arrow is the total flux for ESO 005-G004 for which IRS cannot confidently resolve the AGN component. The 1:1 dependence is shown with the solid line.

(A color version of this figure is available in the online journal.)

in X-ray and infrared luminosities. However, the X-ray uncertainties were estimated in a rather arbitrary way, taking into account long-term variability for some sources but not for others. This led to significantly different weights ascribed to different sources in fitting. In our view, for the problem at hand, it is preferable to use a standard linear regression procedure in log–log space giving equal weights to all the sources in a sample. In fact, Gandhi et al. (2009) did perform such an analysis and obtained a somewhat flatter dependence $L_{12\,\mu m} \propto L_X^{1.02\pm0.07}$, which is, however, still significantly steeper than the $L_{15\,\mu m} \propto L_{HX}^{0.74\pm0.06}$ relation found here.

Another potentially important factor is the use of 2–10 keV X-ray luminosities by Gandhi et al. (2009) versus our use of HX luminosities. Due to our HX selection and the resulting insensitivity to absorption effects, we are able to determine HX luminosities directly from 17–60 keV fluxes measured by *INTEGRAL*. In comparison, the Gandhi et al. (2009) sample contains a large number of significantly absorbed ($N_H \gtrsim 10^{23}\,cm^{-2}$) sources whose intrinsic 2–10 keV luminosities were estimated through model-dependent analysis of X-ray spectra or, in some cases, even using [O III] optical line fluxes. We have compared the HX and X-ray luminosities for 16 Seyfert galaxies (excluding the Compton-thick Seyfert NGC 1068) that are present in both the *INTEGRAL* and Gandhi et al. (2009) samples. The data, spanning the L_{HX} range from 9×10^{41} erg s^{-1} (Cen A) to 1.4×10^{44} erg s^{-1} (Mrk 509), prove to be consistent with L_{HX} being proportional to L_X. The small scatter (0.23 dex) associated with this correlation can be fully attributed to the uncertainties in the L_X values as estimated by Gandhi et al. (2009), whereas the mean ratio $L_{HX}/L_X \approx 1.5$ may be considered typical for AGNs and is only slightly larger than the ratio (1.2) corresponding to a fiducial AGN spectrum used in our analysis below (Section 6.1). Furthermore, systematic studies based on AGNs from the *INTEGRAL* (de Rosa et al. 2012) and *Swift*/BAT (Winter et al. 2009) HX surveys have not
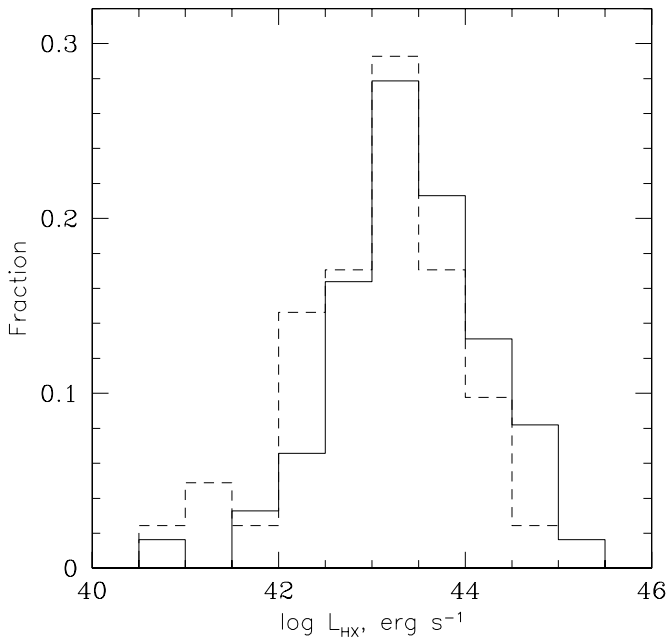
Figure 6. Distribution of AGNs from our clean sample (solid line) and the Gandhi et al. (2009) one (dashed line) over the HX luminosity. For the latter sample we assumed that $L_{HX} = 1.5\,L_X$.

revealed a significant dependence of the HX/X-ray flux ratio on luminosity. We thus conclude that the use of L_X by Gandhi et al. (2009) versus our use of L_{HX} is unlikely to lead to a significant difference between the results of the corresponding X-ray–infrared cross-correlation analyses.

Differences in the infrared data analysis might also play a role. Our study is based on *Spitzer*/IRS spectroscopy and uses a template-based separation of AGN and starburst spectral components. Gandhi et al. (2009) use narrow-filter photometry near rest-frame 12 μm with the VISIR instrument on VLT, which provides a significantly better angular resolution compared to *Spitzer*/IRS and hence presumably minimizes host galaxy contamination. We have again used the overlapping sample of 16 Seyferts to check if there are any systematic differences associated with these two approaches. Specifically, we used our IRS spectra and derived fluxes within the VISIR filters that were used by Gandhi et al. (2009), which differ from object to object. As shown in Figure 5, although the total fluxes measured by IRS spectra are somewhat higher than those measured by VISIR, our standard correction for the host galaxy contamination brings both data sets to nearly perfect agreement. A significant difference (a factor of $\sim$2) is only observed for NGC 3081, but it seems natural to expect some deviations in a sample of 16 objects, given that *Spitzer*/IRS and VLT/VISIR observations were not simultaneous (for the same reason, the 8 μm fluxes measured by IRAC and IRS differ significantly for some of our AGNs; see Section 4.4). Furthermore, there is no trend with either distance or luminosity, although the comparison sample spans distances from 3.6 Mpc (Cen A) to 174 Mpc (ESO 209-G012). We conclude that the differences in the infrared data analysis do not significantly bias our results with respect to those of Gandhi et al. (2009).

Perhaps most importantly, Gandhi et al. (2009) used a heterogeneous sample of 42 Seyfert galaxies, whereas we use a statistically complete and somewhat larger sample. As a result, the Gandhi et al. (2009) sample is significantly shifted to lower luminosities relative to ours (Figure 6): e.g., the corresponding

fractions of AGNs with $L_{HX} > 10^{44}$ erg s^{-1} are 12% and 38%. As was discussed in Section 5.1, dividing our sample into two subsets, $z < 0.02$ and $z > 0.02$, represented by relatively low and high luminosity AGNs, respectively ($\sim$10^{42}–10^{44} versus $\sim$10^{43}–10^{45} erg s^{-1}), tentatively suggests that the slope of the X-ray–infrared correlation changes from 0.93 ± 0.10 to 0.69 ± 0.16 as the AGN luminosity increases. The Gandhi et al. (2009) sample effectively probes the luminosity range $L_{HX} \lesssim 10^{44}$ erg s^{-1}, similar to our $z < 0.02$ subsample, and the slopes inferred for these two data sets are in satisfactory agreement with one another. This suggests that the results of Gandhi et al. (2009) and the present work are actually consistent with each other.

We conclude that further studies using larger, well-defined samples of AGNs are required to clarify if the slope of the X-ray–infrared correlation depends on luminosity, as tentatively suggested by the existing data.

6. TORUS VERSUS DISK AND CORONA

The unified model posits that a torus of molecular gas and dust subtending a solid angle Ω_{Torus} (if viewed from the SMBH) intercepts optical, UV, and soft X-ray radiation from the central accretion flow and converts it into thermal infrared emission. Therefore, assuming that the central source of radiation is isotropic, the total luminosity of the torus is expected to be

$$L_{Torus} \approx \frac{\Omega_{Torus}}{4\pi} L_{Disk}, \qquad (4)$$

where L_{Disk} is the luminosity of the accretion disk, presumably emitted between $\lambda \sim 1\,\mu$m (NIR) and $E \sim 2$ keV (soft X-rays). These boundaries usually separate the MIR, BBB, and HX components (see Section 1) in the SEDs of type 1 AGNs (see, e.g., Elvis et al. 1994; Sazonov et al. 2004). Physically, the 1 μm boundary marks the onset of thermal emission from hot dust at sublimation temperature ($\sim$1500 K), whereas accretion disk emission is expected to peak in the near- or far-UV bands in quasars and Seyfert galaxies (e.g., Shakura & Sunyaev 1973; Hubeny et al. 2001). Therefore, the chosen energy boundaries for L_{Disk} ensure that virtually all of the accretion disk luminosity is accounted for.

Depending on the column density through the torus, it can also reprocess a fraction $\lesssim \Omega_{Torus}/(4\pi)$ of the higher energy (2–10 keV) luminosity emitted by a hot corona of the accretion disk. We have neglected this contribution in Equation (4), first because the torus's optical depth may be significantly smaller than unity for 5–10 keV X-rays, in contrast to the softer emission from the accretion disk, and also because we expect the X-ray (below 10 keV) luminosity of the corona to be much lower than the bolometric luminosity of the accretion disk. This last assumption will be verified below upon completion of our cross-correlation analysis. Finally, it is assumed that none of the HX emission (above 10 keV) is absorbed within the AGN, which is a reasonable assumption except for very Compton-thick objects such as NGC 1068.

As demonstrated below, *Spitzer* and *INTEGRAL* data together make it possible to estimate the luminosity (L_{Torus}) and the solid angle (Ω_{Torus}) of the torus, as well as the luminosity of the corona (at energies 2–300 keV), L_{Corona}. We can therefore use Equation (4) to study the relationship between L_{Disk} and L_{Corona}, i.e., between emission properties of the accretion disk and corona.

6.1. Bolometric Corrections

We proceed by determining coefficients for conversion of the measured quantities L_{HX} and $L_{15\,\mu m}$ to the AGN intrinsic quantities L_{Corona} and L_{Torus}, respectively. HX spectral shapes do not vary much from one Seyfert galaxy to another, apart from the photoabsorption rollover in type 2 objects below 10 keV. Typically, absorption-corrected AGN spectra can be described above 2 keV as a power law with a photon index $\Gamma \sim 1.7$ (e.g., Reeves & Turner 2000) and a rollover above ~ 100 keV (e.g., Molina et al. 2009). We adopt that

$$L_{HX} \approx 0.3\, L_{Corona}. \tag{5}$$

This relation corresponds to a power-law spectrum with $\Gamma = 1.7$ and an exponential cutoff at $E_f = 200$ keV and is consistent with an average 3–300 keV spectrum of ~ 100 local AGNs detected during *INTEGRAL* and *RXTE* surveys of the sky (Sazonov et al. 2008, 2010). Assuming that the values of the power-law index and cutoff energy vary from $\Gamma = 1.5$ to 1.9 and from $E_f \sim 50$ to ~ 500 keV from one Seyfert galaxy to another (as indicated by numerous studies, e.g., Zdziarski et al. 1995; Molina et al. 2009), we can estimate that the conversion described by Equation (5) can introduce a scatter in L_{HX} values for a given L_{Corona} of $\lesssim 20\%$, i.e., $\lesssim 0.1$ dex.

We next introduce a similar correction factor for the reprocessed emission from the torus:

$$L_{15\,\mu m} \approx 0.5\, L_{Torus}. \tag{6}$$

To obtain the above coefficient, we compared the $15\,\mu m$ luminosity with that integrated over the rest-frame $6–32\,\mu m$ band, $L_{6–32\,\mu m}$, for those *Spitzer*/IRS spectra (21 in total) that span this whole wavelength range (i.e., there are available data from the IRS second-order SL module) and do not suffer from significant contamination by MIR emission from dust associated with star formation. For the majority of these objects, the ratio $L_{15\,\mu m}/L_{6–32\,\mu m}$ is bounded in the narrow range of 0.65–0.85, only slightly depending on whether AGN emission lines (such as [O IV] $25.9\,\mu m$) are taken into account or not. We therefore adopted the relation $L_{15\,\mu m}/L_{6–32\,\mu m} = 0.75$ for AGN tori and additionally lowered this ratio by one-third in Equation (6) to account for non-negligible ($\sim 50\%$) additional torus emission both shortward of $6\,\mu m$ and longward of $32\,\mu m$ (see, e.g., Nenkova et al. 2008). While the resulting $L_{15\,\mu m}/L_{Torus}$ ratio (Equation (6)) is determined less strictly than the ratio L_{HX}/L_{Corona} above, the associated scatter in individual $L_{15\,\mu m}/L_{Torus}$ values around the mean trend given by Equation (6) is probably less than 20%, as suggested by the comparison of IRS spectra for "pure" objects, described above.

6.2. Solid Angle of the Torus

The next step in our analysis is to derive the torus solid angle Ω_{Torus}. To this end, we assume that, for a given HX luminosity, Ω_{Torus} is determined by the relative number of obscured (type 2) AGNs of that luminosity, i.e.,

$$\frac{\Omega_{Torus}}{4\pi}(L_{HX}) = \frac{N_{type2}(L_{HX})}{N_{total}(L_{HX})}. \tag{7}$$

We consider an AGN obscured if its X-ray absorption column density $N_H > 10^{22}$ cm^{-2}. In this connection, recall (see Section 2) that the N_H values for our objects are not based on *INTEGRAL* HX measurements but have been determined
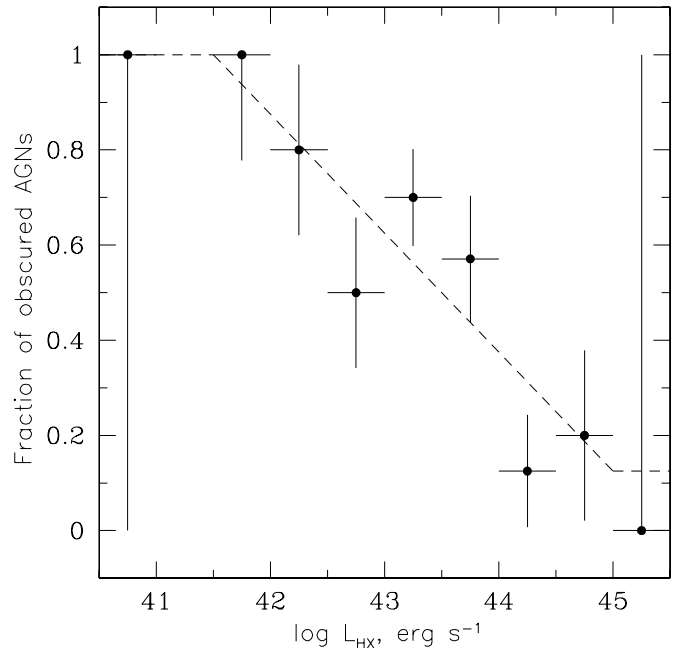

Figure 7. Fraction of obscured ($N_H > 10^{22}$ cm^{-2}) AGNs in the local universe as a function of hard X-ray luminosity, based on the *INTEGRAL* sample. The error bars represent the Poisson uncertainty associated with the number of objects in a given bin. The lowest and highest luminosity bins contain just one source each (NGC 4395 and IGR J09446-2636, respectively). The approximate description of the observed trend by Equation (13) is shown by the dashed line.

through analysis of high-quality X-ray spectra obtained by various X-ray telescopes.

Dividing our AGN sample into several bins in L_{HX}, Figure 7 shows the fraction of absorbed AGNs as a function of L_{HX}. A strong trend of decreasing N_{type2}/N_{total} ratio with increasing luminosity is evident. We can estimate the statistical significance of this trend using a maximum-likelihood estimator,

$$\mathcal{L} = -2 \sum_i \ln P_{1,2}(L_{HX,i}). \tag{8}$$

Here, the summation is over our sample of AGNs and $P_{1,2}$ is the probability for a given object with luminosity $L_{HX,i}$ to be either obscured (P_2) or unobscured (P_1). We restrict our consideration to the luminosity range $41.5 < \log L_{HX} < 45$ because there are only two objects in the sample that fall outside this range (one on either side; see Figure 7). Suppose now that the fraction of obscured AGNs has a power-law dependence on luminosity:

$$P_2 = p + \alpha(\log L_{HX} - 41.5). \tag{9}$$

Obviously,

$$P_1 = 1 - P_2. \tag{10}$$

Requiring that $0 < P_{1,2} < 1$ over the $41.5 < \log L_{HX} < 45$ range yields constraints on the slope and intercept of the trend:

$$0 < p < 1 \tag{11}$$

and

$$-\frac{p}{3.5} < \alpha < \frac{1-p}{3.5}. \tag{12}$$

With these definitions, the maximum of the likelihood function proves to be at $p \approx 1$ and $\alpha = 0.25$. By integrating $\mathcal{L}$ over (p, α) parameter space with the priors given by Equations (11) and (12), i.e., using a Bayesian approach, we find that the

probability that $\alpha < 0$ is 0.999. Hence, the declining luminosity trend of the obscured fraction is ascertained with more than 3σ significance.

Sazonov et al. (2010) have recently confirmed this luminosity dependence (see their Figure 3) using a nearly doubled sample of AGNs detected during 7 years of *INTEGRAL* observations (compared to the 3.5 year all-sky survey used in the present work). Furthermore, the existence of this trend has been reliably established in the past decade using various X-ray-selected samples of AGNs (Ueda et al. 2003; Steffen et al. 2003; Sazonov & Revnivtsev 2004; La Franca et al. 2005; Sazonov et al. 2007; Hasinger 2008; Burlon et al. 2011; see in particular Figure 8 in Hasinger 2008 and Figure 13 in Burlon et al. 2011). Therefore, in accordance with Equation (7) we adopt the expression

$$\frac{\Omega_{\text{Torus}}}{4\pi} = \begin{cases} 1, & \log L_{\text{HX}} \leqslant 41.5 \\ 1 - 0.25(\log L_{\text{HX}} - 41.5), & \\ & 41.5 < \log L_{\text{HX}} < 45 \\ 0.125, & \log L_{\text{HX}} \geqslant 45. \end{cases} \quad (13)$$

We thus assume that the phenomenon of decreasing fraction of absorbed AGNs with increasing luminosity reflects an underlying trend of increasing opening angle of the obscuring torus. This is one of the crucial points in our analysis. According to Equation (13), the slope of the Ω_{Torus} (L_{HX}) dependence is approximately equal to 0.25 for L_{HX} ranging between $\sim 10^{41.5}$ and 10^{45} erg s^{-1} with the associated uncertainty being small, $\sim 10\%$ as determined from the dispersion of data points in Figure 7 and from the Bayesian analysis described above. However, the Ω_{Torus} (L_{HX}) dependence holds true in a statistical sense only, and there might be variations in the torus opening angle among AGNs of a given luminosity. Unfortunately, observations do not yet provide reliable information on the distribution of Ω_{Torus} values for a given L_{HX}, and hence we cannot predict to what degree this scatter could affect our results below. Furthermore, the exact parameters of the $N_{\text{type2}}/N_{\text{total}}$ (L_{HX}) dependence adopted in Equation (13) should be applied only to the local ($z \sim 0$) population of AGNs, in particular because the fraction of obscured sources among high-luminosity AGNs appears to be larger in the distant ($z \gtrsim 1$) universe (e.g., Hickox et al. 2007; Hasinger 2008; Treister et al. 2008).

6.3. Disk versus Corona

We are now ready to estimate the accretion disk luminosities for our AGNs using Equation (4):

$$L_{\text{Disk}} \approx \frac{4\pi}{\Omega_{\text{Torus}}(L_{\text{HX}})} L_{\text{Torus}}. \quad (14)$$

Specifically, we first determine L_{Corona} and L_{Torus} using Equations (5) and (6), respectively, and then use Equation (14) to find L_{Disk}. The resulting scatter plot of L_{Disk} versus L_{Corona} for the clean sample excluding NGC 4395 is shown in Figure 8.

Fitting the L_{Disk} versus L_{Corona} data in Figure 8 with a power law yields the correlation

$$L_{\text{Disk},44} = (1.59 \pm 0.16) L_{\text{Corona},44}^{0.97 \pm 0.06}, \quad (15)$$

where the luminosities are measured in units of 10^{44} erg s^{-1}. The rms scatter around the mean trend is 0.33 and 0.34 dex along the L_{Disk} and L_{Corona} coordinates, respectively.

The derived relation, Equation (15), allows one to predict the disk luminosity for a given coronal luminosity. Hence, if the
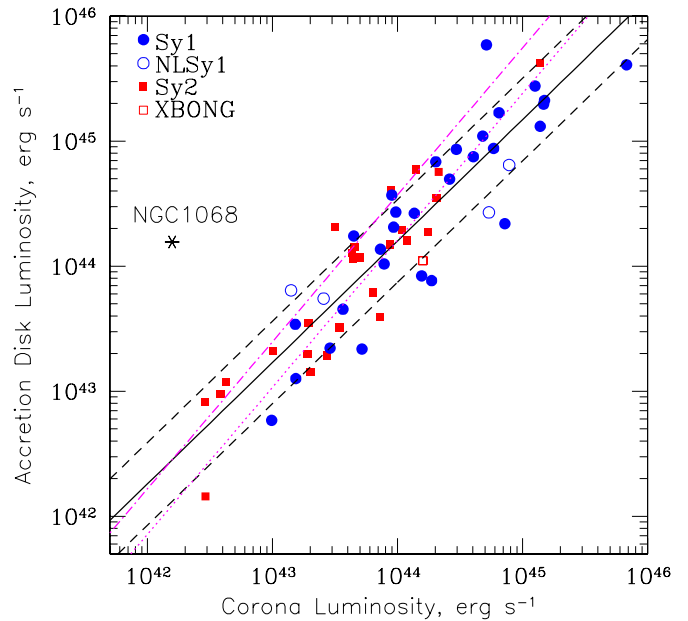

Figure 8. Inferred luminosity of the accretion disk vs. that of the hot corona for the clean sample of 60 AGNs (the LLAGN NGC 4395 is excluded). Various AGN types are indicated by different symbols as in Figure 4. Also shown is the Compton-thick Seyfert 2 galaxy NGC 1068, which was excluded from the analysis. The black solid line is the best-fitting power-law dependence L_{Disk} (L_{Corona}) given by Equation (15), while the two black dashed lines show this dependence multiplied and divided by 2.14, the rms scatter of the correlation. The magenta dotted line is the best-fitting dependence L_{Corona} (L_{Disk}) (Equation (B3)), and the magenta dash-dotted line is the same dependence corrected for the Malmquist bias (Equation (B4)).

(A color version of this figure is available in the online journal.)

coronal luminosity L_{Corona} of an AGN is known, one can expect its accretion disk luminosity to be equal within a factor of ≈ 2 (at the 1σ confidence level) to 1.6 L_{Corona}. The $L_{\text{Disk}}/L_{\text{Corona}}$ ratio does not significantly depend on luminosity in the effective range of L_{Corona} from $\sim 10^{43}$ to 10^{45} erg s^{-1}.

The 2–10 keV energy band contains $\sim 25\%$ of the total coronal luminosity. If all of this X-ray emission were converted in the torus into infrared radiation as efficiently as accretion disk emission, it would increase L_{Torus} by only $\sim 15\%$. This justifies the approximation adopted in Equation (4).

For some applications, one may also be interested in knowing the distribution of L_{Corona} for a given L_{Disk}, rather than L_{Disk} as a function of L_{Corona}. We have therefore also computed (Appendix B) the inverse linear regression, i.e., $\log L_{\text{Corona}}$ as a function of $\log L_{\text{Disk}}$, for our clean sample excluding NGC 4395. As can be seen in Figure 8, this relation is different from the dependence of L_{Disk} on L_{Corona}.

6.4. Scatter around the Mean Trend

Figure 9 shows the distribution of residuals for the $L_{\text{Corona}}-L_{\text{Disk}}$ correlation. Although it is plotted in terms of L_{Corona} deviations, the distribution of $\delta \log L_{\text{Disk}} \equiv \log L_{\text{Disk}} - \langle \log L_{\text{Disk}}(L_{\text{Corona}}) \rangle$ residuals is quite similar. The distribution can be well described by a lognormal function, $dN/d \log L_{\text{Corona}} \propto \exp[-(\delta \log L_{\text{Corona}})^2/2\sigma^2]$, where $\sigma = 0.34$ is the measured rms scatter of the correlation.

Although the observed scatter in the correlation is fairly small, the intrinsic correlation between the corona and disk luminosities in Seyfert galaxies is probably even tighter. Indeed, the 15 μm fluxes measured by *Spitzer*, from which the L_{Disk} values were derived, presumably represent reprocessed accretion disk
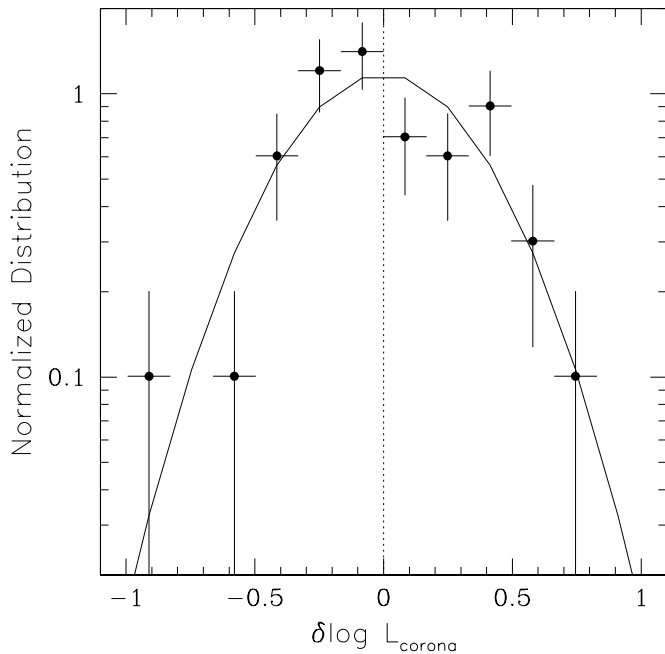
13

Figure 9. Binned distribution of the residuals of the L_{Corona}–L_{Disk} correlation, Equation (15). The error bars represent the Poisson uncertainty associated with the number of objects in a given bin. The solid line shows the lognormal distribution corresponding to the measured rms scatter ($\sigma = 0.34$).

emission averaged over a number of years. Interferometric observations of Seyfert galaxies have established that the size of the MIR-emitting dust region is of the order of several light years or more (Tristram et al. 2009). Specifically, the characteristic size of the 12 μm source was found to scale approximately as the square root of the AGN luminosity[9] and to vary from $l \sim 0.5$ pc for $L_{12\,\mu m} \sim 10^{42}$ erg s^{-1} to $l \sim 50$ pc for $L_{12\,\mu m} \sim 10^{46}$ erg s^{-1}. For example, Tristram et al. (2009) and Tristram & Schartmann (2011) found $l \approx 2$–3 pc for NGC 1068, NGC 1365, MCG 5-23-16, and NGC 4151 and $\sim$10 pc for NGC 7469. Therefore, the L_{Disk} values used in our cross-correlation analysis should represent accretion disk luminosities averaged over the $\sim 2l/c$-long period immediately preceding the *Spitzer* observation of a given AGN, which is expected to range from a few years for the least luminous sources to a few tens of years for the most luminous ones. As demonstrated in Appendix C, variability of the HX coronal emission, detected by *INTEGRAL* on timescales shorter than the characteristic timescale of MIR variations, is expected to induce a scatter of $\sim$0.2–0.25 dex around the mean L_{Corona}–L_{Disk} trend.

Additional contributions to the observed scatter around the mean L_{Corona}–L_{Disk} trend can be provided by systematic uncertainties associated with (1) measurement of L_{HX} and $L_{15\,\mu m}$, each $\lesssim$0.1 dex (see Table 1 and Section 4.4); (2) conversion from L_{HX} to L_{Corona} and from $L_{15\,\mu m}$ to L_{Torus}, also $\lesssim$0.1 dex each (Section 6.1); and (3) determination of the mean torus solid angle (Ω_{Torus}) for a given AGN luminosity and consequently conversion from L_{Torus} to L_{Disk} (via Equation (14)), $\lesssim$0.05 dex (Section 6.2). Hence, each of the above effects can contribute of the order of, or less than, 0.1 dex to the observed scatter in the L_{Corona}–L_{Disk} correlation. Adding these contributions in quadrature to that expected from variability implies that the total induced scatter is $\sim$0.25 dex. After subtraction of this contribution from the measured scatter of the L_{Corona}–L_{Disk} correlation,

---

[9] This is consistent with the simple argument based on considering dust heating by a central source of UV emission (Barvainis 1987).

with rms = 0.33 dex, there remains a scatter $\sim$0.2–0.25 dex, i.e., a factor of 1.5–2.

Therefore, the intrinsic correlation between accretion disk and coronal emission in Seyfert galaxies is fairly tight. Furthermore, neither the L_{Corona}–L_{Disk} relation nor the L_{HX}–$L_{15\,\mu m}$ relation, from which it originates, shows a significant dependence on either optical AGN type or X-ray absorption column density, although there are exceptions, which are discussed below. Assuming that the torus is co-aligned with the accretion disk and is a quasi-isotropic MIR emitter, this suggests that the coronal HX emission is at most modestly (less than a factor of $\sim$2) anisotropic. This conclusion also holds true if the obscuring torus is oriented quasi-randomly with respect to the accretion disk/corona axis because for given $L_{15\,\mu m}$ there is little scatter in L_{HX}. By the same argument, the HX luminosity of AGNs cannot be dominated by collimated emission from relativistic jets.

As to the origin of the remaining (unaccounted for) scatter, at least two effects are likely to contribute to it. First, our analysis was based on the assumption that the characteristic solid angle subtended by the obscuring torus, Ω_{Torus}, is the same for all AGNs of a given luminosity. In reality, it is possible that Ω_{Torus} varies from one object to another (e.g., Elitzur 2012). This would directly affect our estimates of L_{Disk} from L_{Torus} and introduce scatter in the resulting correlation between L_{Corona} and L_{Disk}. Similarly, the amplitude of the Compton reflection component, ignored in our analysis, may vary from one AGN to another, which would introduce additional scatter. Therefore, the scatter in the intrinsic ratio of powers generated in the accretion disk and corona is likely even smaller than 0.2 dex.

6.5. Comparison with Typical Quasars

The results of this work pertain to nearby Seyfert galaxies, and it is interesting to put them into the broader context of the cosmic history of SMBH growth. To this end, we compare our findings with the properties of the SED of the "average quasar" from Sazonov et al. (2004). This template essentially rests on the assumption that the CXB represents the integrated HX emission of all AGNs in the universe and on the argument of Soltan (1982) that the cumulative bolometric luminosity of AGNs is determined by the mean radiative efficiency ϵ with which the integrated mass of local SMBHs has been accumulated over the cosmic time. Adopting $\epsilon = 0.1$, Sazonov et al. (2004) found that $\approx$12.5% of the bolometric luminosity (below 300 keV) of the average quasar is emitted at energies above 2 keV. Attributing this emission to the corona of the accretion disk and making a small correction for absorption in the 2–10 keV energy band (because here we are interested in intrinsic rather than observed properties of accretion disks and coronae), we find that $L_{Disk} \approx 6\,L_{Corona}$ for the average quasar. If we instead assume that $\epsilon = 0.06$, which corresponds to the standard Shakura–Sunyaev disk around a Schwarzschild black hole, then $\langle L_{Disk}/L_{Corona}\rangle \approx 3.5$. By construction, this ratio primarily characterizes quasars with $L_{Corona} \sim 10^{44.5}$ erg s^{-1}, which produce the bulk of the CXB (e.g., Ueda et al. 2003).

We can now determine the corresponding average ratio for the local AGN population, using a completely different method. The mean trend given by Equation (15) and the associated scatter (0.34 dex) imply that the L_{Disk}/L_{Corona} ratio varies between $\approx$0.75 and $\approx$3.4 (the 1σ range) around the mean value of $\approx$1.6. Averaging over the lognormal distribution of L_{Disk}/L_{Corona} yields $\langle L_{Disk}/L_{Corona}\rangle = \int (L_{Disk}/L_{Corona})\,dL_{Disk}/\int dL_{Disk} \approx$ 2.1, independently of L_{Corona}. This ratio characterizes the
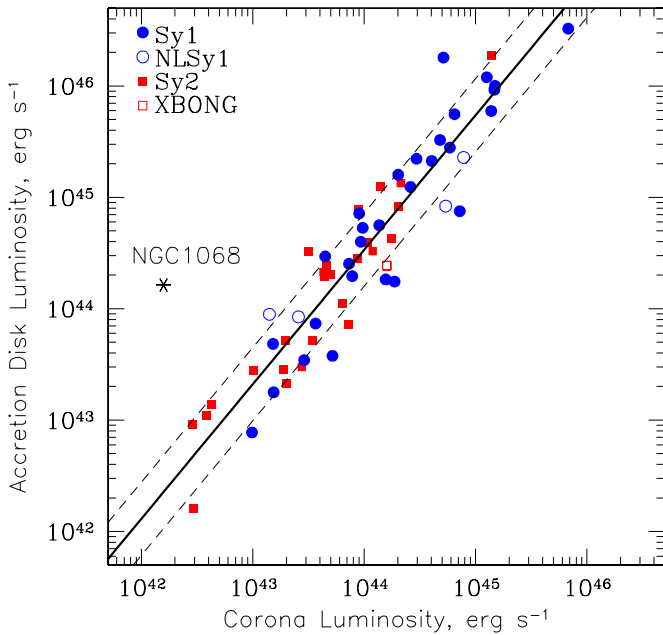
Figure 10. Same as Figure 8, but for an accretion disk emitting according to the cosine law and a dusty torus lying in the plane of the disk. The best-fitting relation is given by Equation (17).

(A color version of this figure is available in the online journal.)

summed radiation of the local AGN population. Therefore, the $\langle L_{\rm Disk}/L_{\rm Corona}\rangle$ ratio appears to be larger, but only by a factor of $\sim$2, for typical quasars making up the CXB relative to typical AGNs in the local universe. This implies that the *ratio of the disk and coronal luminosities is approximately constant in all actively accreting, radiatively efficient SMBHs.*

6.6. Possible Effect of Anisotropic Accretion Disk Emission

Our treatment so far has been based on the assumption that the accretion disk is an isotropic source, i.e., its observed luminosity is independent from the viewing angle. This implies that the primary (UV) and reprocessed (infrared) luminosities of AGNs are related through Equation (4). However, the actual angular distribution of radiation emergent from the accretion disk around an SMBH might be close to Lambert's law, in which case the luminosity per solid angle $dL_{\rm Disk}/d\Omega \propto \cos\theta$, where θ is the viewing angle with respect to the axis of the disk. If, in addition, an obscuring torus is not randomly oriented but its equator lies in the plane of the accretion disk, then there will be a different relation between $L_{\rm Torus}$ and $L_{\rm Disk}$:

$$L_{\rm Torus} \approx \left(\frac{\Omega_{\rm Torus}}{4\pi}\right)^2 L_{\rm Disk}. \qquad (16)$$

Considering this possibility a feasible alternative to our baseline scenario, we repeated our calculations using Equation (16) instead of Equation (4). The resulting correlation between the corona and disk luminosities is shown in Figure 10, and the corresponding best-fitting relation is given by

$$L_{\rm Disk,44} = (3.4 \pm 0.3)L_{\rm Corona,44}^{1.21\pm0.06}, \qquad (17)$$

with the rms scatter $\sigma = 0.33$ in $L_{\rm Disk}$.

The anisotropic scenario predicts significantly larger $L_{\rm Disk}/L_{\rm Corona}$ ratios at high luminosities (a factor of $\sim$3 at $L_{\rm Corona} = 10^{45}$ erg s^{-1}) compared to the isotropic case. However, at these luminosities there is large uncertainty in the inferred $L_{\rm Disk}$ values for the anisotropic case, which is not fully

reflected in the formal uncertainties quoted in Equation (17). Specifically, the uncertainty associated with our adopted dependence of the torus solid angle on luminosity, Equation (13), is not taken into account. As is clear from Figure 7, this additional uncertainty is large at high luminosities, $L_{\rm HX} \gtrsim 10^{44}$ erg s^{-1}, which was relatively unimportant when we considered the isotropic scenario but is the dominant source of uncertainty for the anisotropic scenario due to the quadratic dependence on $\Omega_{\rm Torus}$ in Equation (16).

The above consideration ignores two potentially important effects. First, radiative transfer in the accretion disk may lead to a limb-darkening effect, making the emission even more collimated in the polar direction than $\cos\theta$ (e.g., Sunyaev & Titarchuk 1985; Laor & Netzer 1989). On the other hand, strong gravity in the vicinity of a black hole tends to harden the spectrum and increase the luminosity for observers viewing the accretion disk at grazing angles, with this effect being especially pronounced for rapidly rotating black holes (Cunningham 1975; Malkan 1983).

Taking these various factors into account, it is likely that the correlations obtained in our isotropic (Figure 8) and anisotropic (Figure 10) scenarios bracket the true relationship between the corona and disk emission in AGNs. Furthermore, orientation effects and object-to-object variations in the black hole spin can contribute to the scatter in the relation between $L_{\rm Disk}$ and $L_{\rm Corona}$.

7. DISCUSSION AND CONCLUSIONS

The main result of this work is that the luminosities of the accretion disk and corona are nearly proportional for nearby AGNs: $L_{\rm Disk} \propto L_{\rm Corona}^{0.97\pm0.06}$. To reveal this correlation, we derived intrinsic (presumably emitted between $\lambda \sim 1\,\mu$m and $E \sim 2$ keV) accretion disk luminosities from observed torus luminosities, $L_{\rm Torus}$, using Equation (14), which assumes that radiation from the accretion disk is reprocessed in a dusty torus whose effective solid angle decreases with increasing luminosity from almost 4π at $L_{\rm HX} \sim 10^{42}$ erg s^{-1} to $\sim 4\pi/8$ at $L_{\rm HX} \sim 10^{45}$ erg s^{-1}, as suggested by the observed falling fraction of obscured AGNs (Equations (7) and (13)). This effect of decreasing obscuration fraction is responsible for the MIR/HX luminosity ratio decreasing with increasing AGN luminosity: $L_{15\,\mu{\rm m}} \propto L_{\rm HX}^{0.74\pm0.06}$.

The observed $L_{\rm Corona}$–$L_{\rm Disk}$ relation implies a mean ratio $\langle L_{\rm Disk}/L_{\rm Corona}\rangle \approx 2$ for nearby AGNs. For comparison, for typical quasars producing the CXB, $\langle L_{\rm Disk}/L_{\rm Corona}\rangle \sim 3.5$–6 (see Section 6.5). Hence, HX radiation from accretion disk coronae (with a possible contribution from jets) carries a significant and roughly constant fraction, $\sim$15%–35%, of the bolometric luminosity of SMBHs accreting in radiatively efficient mode (with a possible exception of black holes accreting near the critical Eddington rate; see Section 7.5 below).

7.1. Intrinsic Ratio of Disk and Corona Luminosities

The measured $L_{\rm Disk}/L_{\rm Corona}$ ratio likely overestimates the ratio of the intrinsic UV and HX luminosities produced by the accretion disk and corona, respectively, because roughly half of the luminosity emitted by the corona is intercepted by the disk (and a small additional amount by the obscuring torus) and only $\sim$10%–20% of this radiation (e.g., Haardt & Maraschi 1993) is reflected, while the rest is reprocessed into thermal, softer emission and thus contributes to the disk luminosity. In contrast, it is well known that the corona in Seyfert galaxies

intercepts only a small fraction of the disk's radiation, probably because the corona is patchy (e.g., Zdziarski et al. 1997). Indeed, the measured shapes of the HX spectra of Seyferts imply that the hot corona is characterized by an amplification factor $A \sim 5$–10 (Gilfanov et al. 2000), i.e., the luminosity of the Comptonized HX radiation emergent from the corona is several times the luminosity of the incident soft photons. This would imply that $L_{\mathrm{Disk}} \ll L_{\mathrm{Corona}}$ if the disk were embedded in a homogeneous corona. Since in reality $L_{\mathrm{Disk}} \gtrsim L_{\mathrm{Corona}}$, as suggested by the results of the present study, the presence of a strong BBB in the spectra of type 1 AGNs, and theoretical arguments (e.g., Zdziarski et al. 1997), the solid angle subtended by the corona with respect to the accretion disk must be small, i.e., to a first approximation the corona does not shield the disk from the observer.

On the other hand, the Compton reflection hump is located approximately in our working *INTEGRAL* energy band (17–60 keV) and may significantly contribute to the measured HX flux (see examples of tentatively detected reflection components in *INTEGRAL* spectra of AGNs in de Rosa et al. 2012), so that we likely overestimate the flux of HX radiation coming directly from the corona in our simplistic analysis.

Considering these counteracting effects together, the intrinsic ratio of the disk and coronal luminosities could be a factor of $\lesssim 2$ smaller than the measured $L_{\mathrm{Disk}}/L_{\mathrm{Corona}}$ ratio. This implies that in Seyfert galaxies, approximately equal powers are generated in the accretion disk and hot corona.

7.2. AGN Bolometric Corrections: Current Rate of SMBH Growth

Our results suggest that HX luminosity is a good proxy for bolometric AGN luminosity ($L_{\mathrm{bol}} = L_{\mathrm{Disk}} + L_{\mathrm{Corona}}$), except for extremely Compton-thick sources like NGC 1068. Using Equations (15) and (5), we can estimate the bolometric correction for the 17–60 keV energy band and the associated 1σ range (due to the scatter in the L_{Corona}–L_{Disk} correlation):

$$\frac{L_{\mathrm{bol}}}{L_{\mathrm{HX}}} \approx 9 \ \ (6\text{–}15) \tag{18}$$

in the range $L_{\mathrm{HX}} \sim 10^{42}$–$10^{44.5}$ erg s^{-1}.

The cumulative HX (17–60 keV) luminosity density of nearby AGNs found by integrating their luminosity function measured by *INTEGRAL* at $L_{\mathrm{HX}} \gtrsim 10^{41}$ erg s^{-1} is $(1.2 \pm 0.2) \times 10^{39}$ erg s^{-1} Mpc^{-3} (Sazonov et al. 2007, 2010). Low-luminosity ($L_{\mathrm{HX}} \lesssim 10^{41}$ erg s^{-1}) AGNs may add up to ~50% to this volume emissivity, as follows from cross-correlating the CXB intensity with the local galaxy distribution (e.g., Revnivtsev et al. 2008; Miyaji et al. 1994; Carrera et al. 1995). Using the $L_{\mathrm{bol}}/L_{\mathrm{HX}}$ ratio from Equation (18), the bolometric luminosity density of local AGNs is thus ~$(1$–$3) \times 10^{40}$ erg s^{-1} Mpc^{-3}. This implies that the integrated present-day growth rate of SMBHs is $\dot{M}_{\mathrm{SMBH}}(z = 0) \sim (2$–$5) \times 10^{-6} (0.1/\epsilon) \, M_{\odot}$ yr^{-1} Mpc^{-3}, where ϵ is the average radiative efficiency of accretion. Comparing $\dot{M}_{\mathrm{SMBH}}(z = 0)$ with the total mass density of local SMBHs, $\rho_{\mathrm{SMBH}}(z = 0) \sim (3$–$5) \times 10^{5} \, M_{\odot}$ Mpc^{-3} (Yu & Tremaine 2002; Marconi et al. 2004), the total SMBH mass is currently growing on a timescale ~10 times the age of the universe.

This estimate of the SMBH growth rate does not fully account for the contribution of obscured accretion taking place in Compton-thick ($N_{\mathrm{H}} \gg 10^{24}$ cm^{-2}) AGNs. Moreover, it is valid only for accretion that is occurring in a radiatively efficient mode. In reality, a substantial fraction of SMBH growth at the present epoch may be taking place through a radiatively inefficient mode of accretion, dominated by mechanical rather than radiative energy output (e.g., Churazov et al. 2005; Merloni & Heinz 2008). Therefore, the total SMBH accretion rate may be higher.

We can re-calculate the bolometric correction given by Equation (18) to the standard X-ray band, 2–10 keV. Assuming, as in Section 6.1, a power-law spectrum with $\Gamma = 1.7$ and an exponential cutoff with $E_{\mathrm{f}} = 200$ keV, the 2–10 keV/17–60 keV luminosity ratio $L_{\mathrm{X}}/L_{\mathrm{HX}} = 0.82$ and therefore

$$\frac{L_{\mathrm{bol}}}{L_{\mathrm{X}}} \approx 11 \ \ (7\text{–}18). \tag{19}$$

This formula predicts the bolometric luminosity of an AGN from its intrinsic (i.e., unabsorbed) luminosity in the 2–10 keV energy band in the range $L_{\mathrm{X}} \sim 10^{42}$–$10^{44.5}$ erg s^{-1}.

Finally, we can estimate the bolometric correction for the MIR band ($\lambda = 15 \, \mu$m), using Equations (18) and (3):

$$\frac{L_{\mathrm{bol}}}{L_{15 \, \mu\mathrm{m}}} \approx 5. \tag{20}$$

This formula should be accurate to within a factor of ~2 for AGNs with $L_{15 \, \mu\mathrm{m}} \sim 10^{42}$–$10^{44.5}$ erg s^{-1}. We have not tried to take into account the nonlinear dependence of $L_{15 \, \mu\mathrm{m}}$ on L_{HX}, because it should only be used to predict $L_{15 \, \mu\mathrm{m}}$ for a given L_{HX} but not L_{HX} for a given $L_{15 \, \mu\mathrm{m}}$. A more reliable bolometric correction for the MIR band could be obtained by using an MIR-selected sample of AGNs. Interestingly, Equation (20) is in good agreement with an early estimate by Spinoglio & Malkan (1989), $L_{\mathrm{bol}}/L_{12 \, \mu\mathrm{m}} \sim 5$, based on direct integration of the IR-to-UV ($\lambda = 0.1$–$100 \, \mu$m) spectra of bright Seyfert galaxies. In reality, as we have shown in this paper, the decreasing trend of the MIR/bolometric luminosity ratio with increasing L_{bol} largely arises owing to the decreasing torus angular size, Ω_{Torus}, whereas the $L_{\mathrm{Disk}}/L_{\mathrm{bol}}$ fraction remains nearly constant.

7.3. Comparison with the UV–X-ray Luminosity Relation

A number of studies have found that the ratio of near-UV (~2500 Å) to soft X-ray (~2 keV) luminosities in type 1 AGNs increases with luminosity (e.g., Vignali et al. 2003; Strateva et al. 2005; Steffen et al. 2006; Young et al. 2010; see, however, Yuan et al. 1998; Gaskell et al. 2004; Tang et al. 2007). This suggests that the disk/corona luminosity ratio increases with luminosity, in apparent contradiction to our finding that this ratio is approximately constant over about two decades in luminosity.

Part of the explanation may be that although the near-UV flux might be a good proxy of the bolometric luminosity of the accretion disk in luminous quasars containing very massive black holes, it might be a poor indicator (see also Vasudevan & Fabian 2007; Vasudevan et al. 2009) in lower luminosity AGNs with less massive black holes (such as Seyfert galaxies) because the maximum of their accretion disk emission is expected to be located in the extreme-UV rather than in the near-UV band (e.g., Shakura & Sunyaev 1973; Hubeny et al. 2001). MIR observations, such as used in the present study, make it possible to disclose the true bolometric luminosity of the accretion disk by measuring the luminosity of the obscuring torus, which serves as a calorimeter of the power radiated by the central engine.

Furthermore, there is probably no discrepancy at all because our study probes relatively LLAGNs compared to the quasars used in the $L(2 \, \mathrm{keV})/L(2500 \, \mathrm{Å})$ studies. Indeed, assuming

again a $\Gamma = 1.7$ power-law spectrum with an exponential cutoff at $E_f = 200$ keV, the 10^{42}–$10^{44.5}$ erg s^{-1} luminosity range effectively probed by *INTEGRAL* in the 17–60 keV band corresponds to a range of 2 keV monochromatic luminosities of 9×10^{23}–3×10^{26} erg s Hz^{-1}. As can be seen, e.g., from Figure 4 in Steffen et al. (2006), such AGNs are located in the low-luminosity part of the $L(2500\,\text{Å})$–$L(2\,\text{keV})$ diagram, where the data are consistent with $L(2\,\text{keV})$ being proportional to $L(2500\,\text{Å})$, whereas the evidence for a decreasing luminosity trend of $L(2\,\text{keV})/L(2500\,\text{Å})$ comes from more luminous AGNs with $L(2\,\text{keV}) \gtrsim$ a few $\times 10^{26}$ erg s^{-1} Hz^{-1}. This possible change or gradual evolution of the trend is further suggested by our finding (see Section 6.5) that for typical quasars producing the CXB, with $L(2\,\text{keV}) \sim 2 \times 10^{26}$ erg s^{-1} Hz^{-1}, the $L_{\text{Disk}}/L_{\text{Corona}}$ ratio is about twice that for the *INTEGRAL* sample of (lower luminosity) AGNs.

We conclude that although the reported behavior of the $L(2\,\text{keV})/L(2500\,\text{Å})$ ratio may be indicative of the $L_{\text{Disk}}/L_{\text{Corona}}$ ratio decreasing with luminosity in the most powerful quasars, this trend might be weak or absent in less luminous AGNs. Clearly, further investigation of this issue is required.

7.4. Implications for SMBH Radiative Feedback

The results of the present work have implications for the role of AGN feedback in the co-evolution of SMBHs and galaxies. The observed correlations between the masses of SMBHs and parameters of their host elliptical galaxies/bulges (e.g., Tremaine et al. 2002) are possibly caused by coupling of energy released by the accreting SMBH to gas inside and around its host galaxy. This energy can be supplied in either mechanical (e.g., Churazov et al. 2002; King 2003) or radiative (e.g., Ciotti & Ostriker 2001) form. The latter possibility was considered in detail by Sazonov et al. (2004), who showed that radiation from typical quasars producing the bulk of the CXB is characterized by a Compton temperature[10] of $kT_c \approx 2$ keV. From the *INTEGRAL*/*Spitzer* study we now find, using Equation (1) in Sazonov et al. (2004) and taking into account the scatter in the $L_{\text{Disk}}/L_{\text{Corona}}$ ratio, that for local AGNs kT_c varies between ≈ 2 and 6 keV (note that the quasar SED in Sazonov et al. 2004 extends to MeV energies, while here we do not take into account any radiation emitted above 300 keV).

Thus, radiation from an SMBH can photoionize and Compton heat ambient interstellar gas above the virial temperatures of even giant elliptical galaxies. Therefore, AGN radiative heating can indeed play an important role in the co-evolution of galaxies and SMBHs, as has been suggested previously (Ciotti & Ostriker 2001; Sazonov et al. 2005; Proga et al. 2008; Novak et al. 2011). As discussed below, some studies suggest that the relative luminosity of the corona becomes small for SMBHs accreting near the critical Eddington rate, which would cause the Compton temperature to be relatively low for such actively growing black holes. Therefore, there is a need for a detailed study of the dependence of T_c on the Eddington ratio.

7.5. Dependence of the Corona–Disk Relation on the Eddington Ratio

Vasudevan & Fabian (2007, 2009), using UV and X-ray flux measurements of AGNs and estimates of their black hole

masses, found that the disk/corona luminosity ratio is significantly larger for SMBHs accreting close to the Eddington limit, i.e., having $L_{\text{bol}}/L_{\text{Edd}} \lesssim 1$, relative to objects with $L_{\text{bol}}/L_{\text{Edd}} \ll 1$. However, this result is associated with significant uncertainty (as emphasized by the authors) because the estimation of the intrinsic (unabsorbed) luminosity of an accretion disk is difficult even using UV data.

It might be possible to reconcile the near constancy of the $L_{\text{Disk}}/L_{\text{Corona}}$ ratio found in our work (a similar conclusion also follows from the study by Vasudevan et al. 2010, who analyzed *IRAS* infrared data for a *Swift*/BAT sample of AGNs) with the strong dependence of this ratio on $L_{\text{bol}}/L_{\text{Edd}}$ inferred by Vasudevan & Fabian (2007, 2009) if we take into account the fact that most of the *INTEGRAL* (and *Swift*) AGNs have relatively low Eddington ratios (Khorunzhev et al. 2012). On the other hand, a few of our objects, in particular the narrow-line Seyfert galaxies, have $L_{\text{bol}}/L_{\text{Edd}} \lesssim 1$ but nevertheless occupy the same locus on the L_{Corona}–L_{Disk} diagram as the other objects (Figure 8). This seems to argue against a strong dependence of $L_{\text{Disk}}/L_{\text{Corona}}$ on the Eddington ratio. However, there is also a possibility that the effective solid angle of the obscuring torus explicitly depends on (decreases with) the $L_{\text{bol}}/L_{\text{Edd}}$ ratio, which would affect our estimates of the accretion disk luminosity based on the infrared luminosity of the torus.

In future work, an infrared–X-ray cross-correlation study based on the *INTEGRAL* sample of local (relatively low $L_{\text{bol}}/L_{\text{Edd}}$ ratio) Seyfert galaxies complemented by a representative sample of high $L_{\text{bol}}/L_{\text{Edd}}$ ratio quasars could help to clarify how the disk/corona luminosity ratio depends on the Eddington ratio.

APPENDIX A

IRS SPECTROSCOPY VERSUS IRAC PHOTOMETRY

To verify our conclusions about host galaxy contamination of IRS spectra, we can compare 8 μm photometric measurements in small (2${''}$.4) and large (12${''}$) IRAC apertures. The result should depend on the extent of a starburst. If a star formation region is more compact than the small (2${''}$.4) photometric aperture, there should be no significant associated extended 8 μm flux. In the opposite case of a starburst extending over $\gtrsim 10{''}$, i.e., beyond both the large IRAC aperture and the IRS extraction aperture, each 10% starburst contribution to the AGN spectrum at 15 μm should add ~ 30% to the ratio of 8 μm fluxes in the 12${''}$ and 2${''}$.4 apertures, as follows from the comparison of our adopted starburst spectral template (Brandl et al. 2006) with a typical AGN spectrum (taking into account that there are strong 7.7 μm

---

[10] The Compton temperature is the temperature of a gas interacting with a radiation field at which there is no net energy exchange by Compton scattering between photons and electrons.
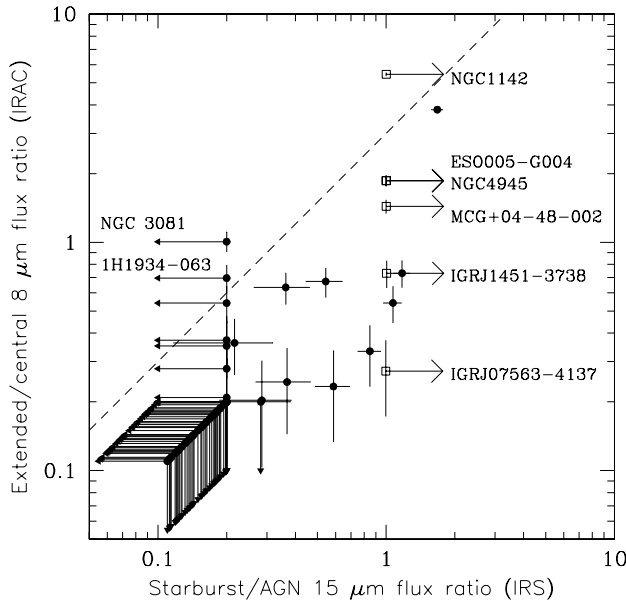
Figure 11. Starburst/AGN $15\,\mu$m flux ratio inferred from IRS spectra vs. extended/compact $8\,\mu$m flux ratio determined by IRAC photometry in $12''$ and $2\overset{''}{.}4$ apertures (with estimated starlight contribution subtracted from the extended flux). Filled circles denote objects from the clean sample (with AGN-dominated spectra). Non-detections ($<2\sigma$) in either of the two quantities are shown as upper limits of 20% (shifted a little apart from each other in the lower left corner of the figure for better visibility). Empty squares denote the six objects with starburst-dominated IRS spectra for which the starburst/AGN $15\,\mu$m flux ratio is of the order of 1:1 or larger. The dashed line indicates the $\sim$3:1 extended/compact flux ratio expected for a sum of the adopted starburst template (Brandl et al. 2006) and a typical AGN spectrum in the case of an extended star formation region.

and $8.6\,\mu$m PAH features falling into the $8\,\mu$m IRAC filter). In addition, there might be a non-negligible contribution of host galaxy starlight to the IRAC extended flux at $8\,\mu$m. In fact, extended stellar emission is clearly seen by IRAC in most of our sources, including "pure" AGNs, at wavelengths $\lambda \lesssim 5\,\mu$m (see Figure 1). The starlight contribution to the extended flux at $8\,\mu$m can be roughly estimated as the extended $3.6\,\mu$m flux multiplied by $(3.6/8)^2$ (i.e., assuming a Rayleigh–Jeans spectrum).

Figure 11 demonstrates that almost all of the sources fulfill the above expectation, namely, the extended/compact $8\,\mu$m flux ratio is less than $\sim$3 times the starburst/AGN spectral flux ratio at $15\,\mu$m. The positions of the sources in the IRS–IRAC diagram probably reflect different angular sizes of their starbursts: the further an object is located below the 3:1 limiting line the more compact is its star formation region. Two sources, 1H 1934−063 and NGC 3081, lie somewhat above the 3:1 boundary in the IRS–IRAC diagram. This apparent discrepancy probably arises because infrared spectral shapes of both starbursts and AGNs should in fact differ from one object to another; hence, there may be a significant scatter around the $\sim$3:1 relation between the starburst fractional contributions at 8 and $15\,\mu$m. We conclude that there is good overall agreement between signatures of host galaxy contamination found by IRS spectroscopy and by IRAC photometry for our objects.

APPENDIX B

INVERSE CORRELATIONS

The derived $L_{15\,\mu\text{m}}$ (L_{HX}) relation, Equation (3), makes it possible to predict the HX luminosity for a given MIR luminosity. For some applications, one may also be interested

in knowing the distribution of L_{HX} for a given $L_{15\,\mu\text{m}}$. We have therefore also computed an inverse linear regression, i.e., $\log L_{\text{HX}}$ as a function of $\log L_{15\,\mu\text{m}}$, for our clean sample excluding NGC 4395:

$$L_{\text{HX},43} = (0.81 \pm 0.13)L_{15\,\mu\text{m},43}^{0.98\pm0.08}. \qquad \text{(B1)}$$

The rms scatter of L_{HX} around the mean trend is 0.39 dex. As can be seen in Figure 2, this relation is different from the dependence of $L_{15\,\mu\text{m}}$ on L_{HX}.

The dependence given by Equation (B1) is expected to be affected by the Malmquist bias. Indeed, our AGN sample is HX selected. Therefore, if for a given MIR luminosity $L_{15\,\mu\text{m}}$ there is a range of possible HX luminosities L_{HX}, the *INTEGRAL* survey would find more objects toward the higher boundary of this range than toward its lower boundary because the more luminous objects can be detected from larger distances and hence from a larger volume of the universe. For example, if for a fixed $L_{15\,\mu\text{m}}$, L_{HX} varies from object to object from L_1 to $L_2 = 4L_1$, then the survey will find $4^{3/2} = 8$ times as many L_2 sources as L_1 sources. The intrinsic correlation can be found following Vikhlinin et al. (2009) by shifting the observed one (Equation (B1)) by $\Delta \log L_{\text{HX}} = -3/2 \times \ln 10 \times \sigma^2 = -0.53$, where $\sigma = 0.39$ is the measured rms scatter in $\log L_{\text{HX}}$. This results in

$$L_{\text{HX},43}(\text{corrected}) = (0.24 \pm 0.04)L_{15\,\mu\text{m},43}^{0.98\pm0.08}. \qquad \text{(B2)}$$

We can also compute the inverse relation between L_{Disk} and L_{Corona} for our clean sample excluding NGC 4395:

$$L_{\text{Corona},44} = (0.67 \pm 0.06)L_{\text{Disk},44}^{0.85\pm0.05}. \qquad \text{(B3)}$$

It is also affected by the Malmquist bias. The intrinsic correlation can be found by shifting the observed one (Equation (B3)) by $\Delta \log L_{\text{Corona}} = -3/2 \times \ln 10 \times \sigma^2 = -0.33$ (where $\sigma = 0.31$ is the measured rms scatter in $\log L_{\text{Corona}}$):

$$L_{\text{Corona},44}(\text{corrected}) = (0.31 \pm 0.03)L_{\text{Disk},44}^{0.85\pm0.05}. \qquad \text{(B4)}$$

Although the inverse relations, Equations (B2) and (B4), are formally correct, they should be used with caution because the implemented corrections for the Malmquist bias are comparable to or larger than the intrinsic scatter in the correlations (see Figures 2 and 8). The inverse relations could be obtained more reliably using an MIR-flux-selected sample of AGNs.

APPENDIX C

EFFECT OF X-RAY VARIABILITY ON THE DERIVED CORRELATIONS

The coronal emission detected by *INTEGRAL* is expected to be substantially variable on timescales much shorter than the characteristic timescale of MIR variations, and this should affect the observed L_{Corona}–L_{Disk} correlation. Indeed, Seyfert galaxies are known to be strongly variable in X-rays on timescales as short as minutes and more so on timescales of months and years (see, e.g., Uttley et al. 2002). To roughly estimate the effect of this variability on the L_{Corona}–L_{Disk} correlation, we have constructed long-term (1996–2009) light curves in the 3–20 keV and 17–60 keV energy bands of several bright, frequently observed AGNs from our sample using *RXTE*/PCA and *INTEGRAL*/IBIS data, respectively.
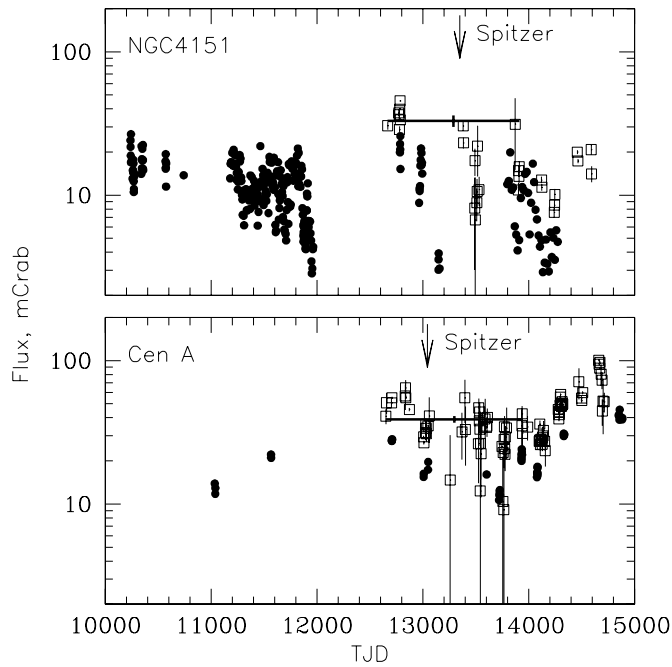
Figure 12. Illustration of the effect of source variability on the L_{Corona}–L_{Disk} correlation. Shown are the long-term light curves of NGC 4151 and Cen A in the 3–20 keV (*RXTE*/PCA, filled circles) and 17–60 keV (*INTEGRAL*/IBIS, open squares) energy bands. The sampling time is 1 and 3 days for *RXTE* and *INTEGRAL*, respectively. Also indicated are the "average" *INTEGRAL* fluxes, f_{HX}, and the periods used for their estimation (thick crosses), as well as the dates of the $f_{15\,\mu\mathrm{m}}$ measurements by *Spitzer* (arrows). Both f_{HX} and $f_{15\,\mu\mathrm{m}}$ have been used in the MIR–HX cross-correlation analysis. Since the MIR data represent the accretion disk emission averaged over the preceding period of a few years or longer, which does not coincide with the period over which the average HX flux was determined, it is clear that there should be significant associated scatter in the L_{Corona}–L_{Disk} correlation.
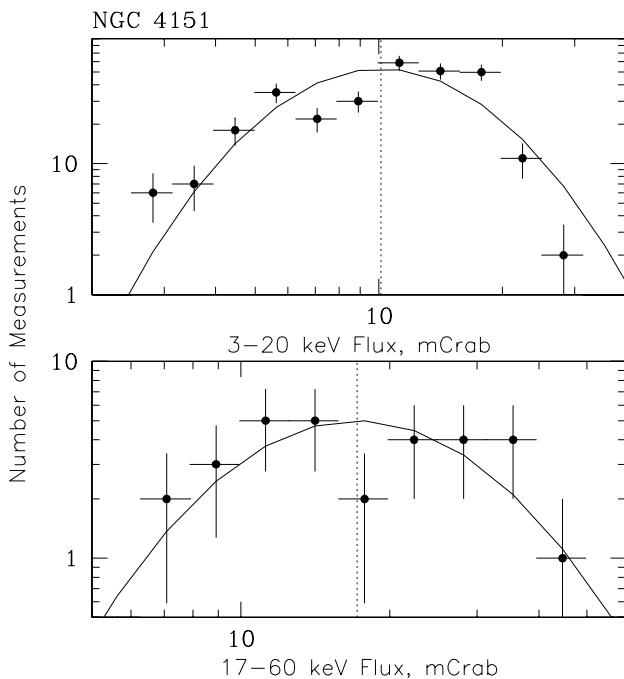

Figure 13. Binned distribution around the log-mean value of individual flux measurements for NGC 4151 by *RXTE*/PCA in the 3–20 keV energy band (upper panel) and by *INTEGRAL*/IBIS in the 17–60 keV band (lower panel). The solid line shows the lognormal distribution with a standard deviation equal to the actually measured rms scatter, 0.22 dex in the 3–20 keV band and 0.24 in the 17–60 keV band.
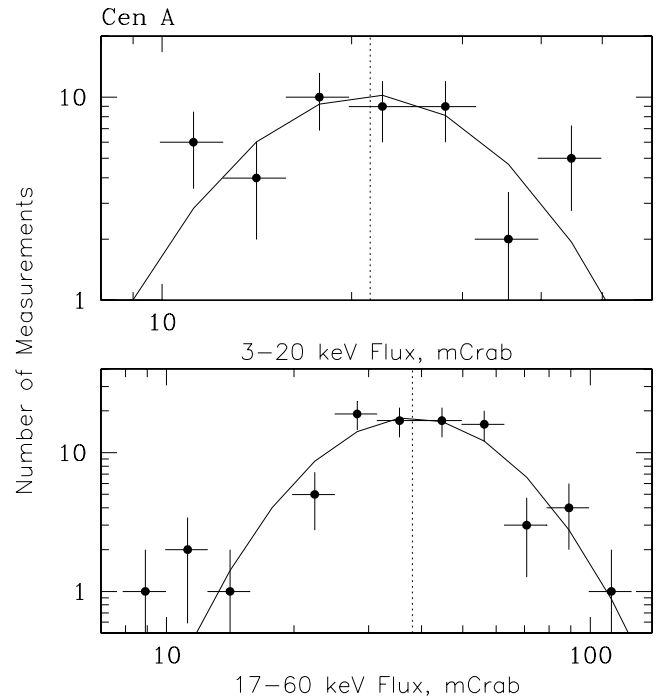

Figure 14. Same as Figure 13, but for Cen A. The rms scatter around the mean log F is 0.17 and 0.19 dex in the 3–20 keV and 17–60 keV energy bands, respectively.

Figure 12 shows the light curves of NGC 4151 and Cen A, the two brightest AGNs in our sample. The (longer and better sampled) *RXTE* light curves demonstrate that the 3–20 keV fluxes of both sources varied by an order of magnitude over a time span of a decade. The same variability behavior is confirmed by the *INTEGRAL* data taken since 2002. The X-ray and HX variations are quantified in Figures 13 and 14, which show the distribution of individual flux measurements, binned in log of flux. The observed flux distributions for NGC 4151 and Cen A can be well described as lognormal with $\sigma = 0.22$–0.24 and 0.17–0.19 dex, respectively. This result is consistent with a number of previous studies that have demonstrated that X-ray flux variations in AGNs, similarly to X-ray binaries, can be described by a lognormal distribution (Gaskell 2004; Uttley et al. 2005).

The majority of AGNs in our sample were observed by *INTEGRAL* only occasionally, typically once a year for a duration of a few days; hence, the HX fluxes measured during 2002–2006, which are used in our cross-correlation analysis, in fact represent random snapshots of sources rather than their long-term averaged fluxes. Therefore, if NGC 4151 and Cen A are typical of the whole sample, X-ray variability should induce a scatter of ∼0.2–0.25 dex around the mean L_{Corona}–L_{Disk} trend. To further illustrate this point, HX fluxes averaged over a more recent period of *INTEGRAL* observations, from 2006–2009, give a factor of ∼2 smaller L_{Corona} for NGC 4151 and a factor of ∼1.5 larger L_{Corona} for Cen A.

REFERENCES

Alonso-Herrero, A., Pereira-Santaella, M., Rieke, G. H., & Rigopoulou, D. 2012, ApJ, 744, 2
Alonso-Herrero, A., Ramos Almeida, C., Mason, R., et al. 2011, ApJ, 736, 82
Antonucci, R. 1993, ARA&A, 31, 473
Barvainis, R. 1987, ApJ, 320, 537
Brandl, B. R., Bernard-Salas, J., Spoon, H. W. W., et al. 2006, ApJ, 653, 1129
Buchanan, C. L., Gallimore, J. F., O'Dea, C. P., et al. 2006, AJ, 132, 401
Burlon, D., Ajello, M., Greiner, J., et al. 2011, ApJ, 728, 58

Carrera, F. J., Barcons, X., Butcher, J. A., et al. 1995, MNRAS, 275, 22
Churazov, E., Sazonov, S., Sunyaev, R., et al. 2005, MNRAS, 363, L91
Churazov, E., Sunyaev, R., Forman, W., & Böhringer, H. 2002, MNRAS, 332, 729
Ciotti, L., & Ostriker, J. P. 2001, ApJ, 551, 131
Cunningham, C. T. 1975, ApJ, 202, 788
Dale, D. A., Smith, J. D. T., Schlawin, E. A., et al. 2009, ApJ, 693, 1821
Deo, R. P., Richards, G. T., Crenshaw, D. M., & Kraemer, S. B. 2009, ApJ, 705, 14
de Rosa, A., Panessa, F., Bassani, L., et al. 2012, MNRAS, 420, 2087
Diamond-Stanic, A. M., & Rieke, G. H. 2010, ApJ, 724, 140
Draine, B. T. 2003, ARA&A, 41, 241
Dullemond, C. P., & van Bemmel, I. M. 2005, A&A, 436, 47
Elitzur, M. 2012, ApJ, 747, L33
Elvis, M., Wilkes, B. J., McDowell, J. C., et al. 1994, ApJS, 95, 1
Fazio, G. G., Hora, J. L., Allen, L. E., et al. 2004, ApJS, 154, 10
Gandhi, P., Horst, H., Smette, A., et al. 2009, A&A, 502, 457
Gaskell, C. M. 2004, ApJ, 612, L21
Gaskell, C. M., Goosmann, R. W., Antonucci, R. R. J., & Whysong, D. H. 2004, ApJ, 616, 147
Gilfanov, M., Churazov, E., & Revnivtsev, M. 2000, in Proc. 5th Sino-German Workshop on Astrohpysics, 1999, ed. G. Zhao, J.-J. Wang, H. M. Qiu, & G. Boerner (SGSC Conference Series, Vol. 1; Beijing: China Science & Technology Press), 114
Goulding, A. D., & Alexander, D. M. 2009, MNRAS, 398, 1165
Goulding, A. D., Alexander, D. M., Bauer, F. E., et al. 2012, ApJ, 755, 5
Goulding, A. D., Alexander, D. M., Mullaney, J. R., et al. 2011, MNRAS, 411, 1231
Haardt, F., & Maraschi, L. 1993, ApJ, 413, 507
Hasinger, G. 2008, A&A, 490, 905
Hickox, R. C., Jones, C., Forman, W. R., et al. 2007, ApJ, 671, 1365
Hönig, S. F., Beckert, T., Ohnaka, K., & Weigelt, G. 2006, A&A, 452, 459
Hönig, S. F., Kishimoto, M., Gandhi, P., et al. 2010, A&A, 515, A23
Horst, H., Smette, A., Gandhi, P., & Duschl, W. J. 2006, A&A, 457, L17
Houck, J. R., Roellig, T. L., van Cleve, J., et al. 2004, ApJS, 154, 18
Hubeny, I., Blaes, O., Krolik, J. H., & Agol, E. 2001, ApJ, 559, 680
Khorunzhev, G., Sazonov, S., Burenin, R., & Tkachenko, A. 2012, Astron. Lett., 38, 539
King, A. 2003, ApJ, 596, L27
Kishimoto, M., Hönig, S. F., Antonucci, R., et al. 2009, A&A, 507, L57
Kozłowski, S., Kochanek, C. S., Stern, D., et al. 2010, ApJ, 716, 530
Krivonos, R., Revnivtsev, M., Lutovinov, A., et al. 2007, A&A, 475, 775
La Franca, F., Fiore, F., Comastri, A., et al. 2005, ApJ, 635, 864
Landi, R., Malizia, A., Masetti, N., et al. 2007, ATel, 1274, 1
Lanzuisi, G., Piconcelli, E., Fiore, F., et al. 2009, A&A, 498, 67
Laor, A., & Netzer, H. 1989, MNRAS, 238, 897
Lutz, D., Maiolino, R., Spoon, H. W. W., & Moorwood, A. F. M. 2004, A&A, 418, 465
Malizia, A., Bassani, L., Bird, A. J., et al. 2008, MNRAS, 389, 1360
Malizia, A., Bassani, L., Panessa, F., de Rosa, A., & Bird, A. J. 2009, MNRAS, 394, L121
Malkan, M. A. 1983, ApJ, 268, 582
Malkan, M. A., & Sargent, W. L. W. 1982, ApJ, 254, 22
Marconi, A., Risaliti, G., Gilli, R., et al. 2004, MNRAS, 351, 169
Masetti, N., Mason, E., Morelli, L., et al. 2008, A&A, 482, 113
Mason, R. E., Geballe, T. R., Packham, C., et al. 2006, ApJ, 640, 612
Matt, G., Fabian, A. C., Guainazzi, M., et al. 2000, MNRAS, 318, 173
Merloni, A., & Heinz, S. 2008, MNRAS, 388, 1011
Miyaji, T., Lahav, O., Jahoda, K., & Boldt, E. 1994, ApJ, 434, 424
Molina, M., Bassani, L., Malizia, A., et al. 2009, MNRAS, 399, 1293
Moran, E. C., Filippenko, A. V., Ho, L. C., et al. 1999, PASP, 111, 801
Mullaney, J. R., Alexander, D. M., Goulding, A. D., & Hickox, R. C. 2011, MNRAS, 414, 1082
Mullaney, J. R., Alexander, D. M., Huynh, M., Goulding, A. D., & Frayer, D. 2010, MNRAS, 401, 995
Mushotzky, R. 2004, in Supermassive Black Holes in the Distant Universe, ed. A. J. Barger (Astrophysics and Space Science Library, Vol. 308; Dordrecht: Kluwer), 53
Nenkova, M., Sirocky, M. M., Nikutta, R., Ivezić, Ž., & Elitzur, M. 2008, ApJ, 685, 160
Netzer, H., Lutz, D., Schweitzer, M., et al. 2007, ApJ, 666, 806
Novak, G. S., Ostriker, J. P., & Ciotti, L. 2011, ApJ, 737, 26
O'Dowd, M. J., Schiminovich, D., Johnson, B. D., et al. 2009, ApJ, 705, 885
Peterson, B. M., Bentz, M. C., Desroches, L.-B., et al. 2005, ApJ, 632, 799
Petric, A. O., Armus, L., Howell, J., et al. 2011, ApJ, 730, 28
Polletta, M. d. C., Wilkes, B. J., Siana, B., et al. 2006, ApJ, 642, 673
Proga, D., Ostriker, J. P., & Kurosawa, R. 2008, ApJ, 676, 101

Reeves, J. N., & Turner, M. J. L. 2000, MNRAS, 316, 234
Revnivtsev, M., Molkov, S., & Sazonov, S. 2008, A&A, 483, 425
Richards, G. T., Lacy, M., Storrie-Lombardi, L. J., et al. 2006, ApJS, 166, 470
Roche, P. F., Aitken, D. K., Smith, C. H., & Ward, M. J. 1991, MNRAS, 248, 606
Rodriguez, J., Tomsick, J. A., & Chaty, S. 2008, A&A, 482, 731
Rodríguez-Ardila, A., Binette, L., Pastoriza, M. G., & Donzelli, C. J. 2000, ApJ, 538, 581
Sales, D. A., Pastoriza, M. G., & Riffel, R. 2010, ApJ, 725, 605
Sazonov, S., Churazov, E. M., Krivonos, R., Revnivtsev, M., & Sunyaev, R. 2010, in Eighth Integral Workshop, The Restless Gamma-ray Universe (INTEGRAL 2010), ed. L. Hanlon, http://pos.sissa.it/cgi-bin/reader/conf.cgi?confid=115
Sazonov, S., Krivonos, R., Revnivtsev, M., Churazov, E., & Sunyaev, R. 2008, A&A, 482, 517
Sazonov, S., Ostriker, J. P., Ciotti, L., & Sunyaev, R. 2005, MNRAS, 358, 168
Sazonov, S., Ostriker, J. P., & Sunyaev, R. 2004, MNRAS, 347, 144
Sazonov, S., Revnivtsev, M., Burenin, R., et al. 2008, A&A, 487, 509
Sazonov, S., Revnivtsev, M., Krivonos, R., Churazov, E., & Sunyaev, R. 2007, A&A, 462, 57
Sazonov, S. Y., & Revnivtsev, M. G. 2004, A&A, 423, 469
Scott, J. E., Kriss, G. A., Brotherton, M., et al. 2004, ApJ, 615, 135
Shakura, N. I., & Sunyaev, R. A. 1973, A&A, 24, 337
Shang, Z., Brotherton, M. S., Wills, B. J., et al. 2011, ApJS, 196, 2
Shi, Y., Rieke, G. H., Hines, D. C., et al. 2006, ApJ, 653, 127
Smith, J. D. T., Armus, L., Dale, D. A., et al. 2007, PASP, 119, 1133
Smith, J. D. T., Draine, B. T., Dale, D. A., et al. 2007, ApJ, 656, 770
Soltan, A. 1982, MNRAS, 200, 115
Spinoglio, L., & Malkan, M. A. 1989, ApJ, 342, 83
Steffen, A. T., Barger, A. J., Cowie, L. L., Mushotzky, R. F., & Yang, Y. 2003, ApJ, 596, L23
Steffen, A. T., Strateva, I., Brandt, W. N., et al. 2006, AJ, 131, 2826
Strateva, I. V., Brandt, W. N., Schneider, D. P., Vanden Berk, D. G., & Vignali, C. 2005, AJ, 130, 387
Sturm, E., Lutz, D., Verma, A., et al. 2002, A&A, 393, 821
Suganuma, M., Yoshii, Y., Kobayashi, Y., et al. 2006, ApJ, 639, 46
Sunyaev, R. A., & Titarchuk, L. G. 1985, A&A, 143, 374
Tang, S. M., Zhang, S. N., & Hopkins, P. F. 2007, MNRAS, 377, 1113
Treister, E., Krolik, J. H., & Dullemond, C. 2008, ApJ, 679, 140
Tremaine, S., Gebhardt, K., Bender, R., et al. 2002, ApJ, 574, 740
Tristram, K. R. W., Raban, D., Meisenheimer, K., et al. 2009, A&A, 502, 67
Tristram, K. R. W., & Schartmann, M. 2011, A&A, 531, A99
Tueller, J., Baumgartner, W. H., Markwardt, C. B., et al. 2010, ApJS, 186, 378
Tully, R. B. 1988, Nearby Galaxies Catalogue (Cambridge: Cambridge Univ. Press)
Tully, R. B., Rizzi, L., Shaya, E. J., et al. 2009, AJ, 138, 323
Ubertini, P., Lebrun, F., Di Cocco, G., et al. 2003, A&A, 411, L131
Ueda, Y., Akiyama, M., Ohta, K., & Miyaji, T. 2003, ApJ, 598, 886
Ueda, Y., Eguchi, S., Terashima, Y., et al. 2007, ApJ, 664, L79
Uttley, P., McHardy, I. M., & Papadakis, I. E. 2002, MNRAS, 332, 231
Uttley, P., McHardy, I. M., & Vaughan, S. 2005, MNRAS, 359, 345
Vasudevan, R. V., & Fabian, A. C. 2007, MNRAS, 381, 1235
Vasudevan, R. V., & Fabian, A. C. 2009, MNRAS, 392, 1124
Vasudevan, R. V., Fabian, A. C., Gandhi, P., Winter, L. M., & Mushotzky, R. F. 2010, MNRAS, 402, 1081
Vasudevan, R. V., Mushotzky, R. F., Winter, L. M., & Fabian, A. C. 2009, MNRAS, 399, 1553
Vaughan, S., Iwasawa, K., Fabian, A. C., & Hayashida, K. 2005, MNRAS, 356, 524
Vignali, C., Brandt, W. N., & Schneider, D. P. 2003, AJ, 125, 433
Vikhlinin, A., Burenin, R. A., Ebeling, H., et al. 2009, ApJ, 692, 1033
Voit, G. M. 1992, MNRAS, 258, 841
Weedman, D. W., Hao, L., Higdon, S. J. U., et al. 2005, ApJ, 633, 706
Werner, M. W., Roellig, T. L., Low, F. J., et al. 2004, ApJS, 154, 1
Winkler, C., Courvoisier, T. J.-L., Di Cocco, G., et al. 2003, A&A, 411, L1
Winter, L. M., Mushotzky, R. F., Reynolds, C. S., & Tueller, J. 2009, ApJ, 690, 1322
Wu, Y., Charmandaris, V., Huang, J., Spinoglio, L., & Tommasin, S. 2009, ApJ, 701, 658
Young, M., Elvis, M., & Risaliti, G. 2010, ApJ, 708, 1388
Yu, Q., & Tremaine, S. 2002, MNRAS, 335, 965
Yuan, W., Siebert, J., & Brinkmann, W. 1998, A&A, 334, 498
Zdziarski, A. A., Johnson, W. N., Done, C., Smith, D., & McNaron-Brown, K. 1995, ApJ, 438, L63
Zdziarski, A. A., Johnson, W. N., Poutanen, J., Magdziarz, P., & Gierlinski, M. 1997, in The Transparent Universe (ESA SP-382), ed. C. Winkler, T. J.-L. Courvoisier, & P. Durouchoux (Noordwijk: ESA), 373
Zhou, H., Wang, T., Yuan, W., et al. 2007, ApJ, 658, L13